# Observation of combined spin-mass vortices in rotating $^3$He-$B$

J. S. Korhonen,* Y. Kondo,† M. Krusius, E. V. Thuneberg, and G. E. Volovik‡
*Low Temperature Laboratory, Helsinki University of Technology, 02150 Espoo, Finland*
(Received 17 August 1992; revised manuscript received 11 December 1992)

We have observed spin-mass vortices (SMV) in rotating superfluid $^3$He-$B$. The SMV is a combined topological object formed of an ordinary vortex with mass current and of a disclination with spin current. A planar defect, so-called $\theta$ soliton, is topologically bound to the SMV line. The SMV's were created primarily by cooling the $^3$He sample through a reversible $A \rightarrow B$ transition at a constant rotation velocity, which was smaller than the critical velocity for the nucleation of vortices in $^3$He-$B$. The observation of the SMV's is based on changes in the NMR absorption caused by the attached solitons: The absorption is shifted to higher frequencies in conventional NMR at low rf excitation and large additional absorption is observed in the homogeneously precessing domain (HPD) at high excitation. The presence of SMV's is deduced from the stability and from the rotation-speed dependence of the additional absorption.

## I. INTRODUCTION

Vortices with quantized mass flow are formed in superfluids by rotation. These line defects have been studied actively in the $A$ and $B$ phases of superfluid $^3$He during the past 10 years. Two vortices, which differ in the structure of their core, have been detected in the $B$ phase.[1,2] In this paper we present experimental results which can be explained by introducing a third vortex in $^3$He-$B$. The defect carries mass flow like an ordinary vortex, called mass vortex (MV) here, but it has also spin superflow around the vortex line. We call it a spin-mass vortex (SMV).

The nucleation of $B$-phase vortices can be suppressed in suitable conditions by a high-energy barrier. Earlier experiments have shown that it is possible to prepare a rotating state which contains considerably fewer than the equilibrium number of vortices.[3] These nonequilibrium states cause distinctive features both in conventional NMR at low rf levels[3,4] and in the so-called homogeneously precessing domain, HPD,[5–7] with large deviation of the magnetization from the direction of the applied magnetic field.[8–10] Here we report on nonequilibrium vortex states whose NMR properties cannot be explained by a vortex deficit alone. In these anomalous states, part of the absorption in the conventional NMR spectrum moves to a peak at the maximum frequency shift, and an additional absorption contribution is measured in the HPD mode.

A model, which can explain the anomalous state, is sketched in Fig. 1. Because there is a deficit in the number of vortices, an annular vortex-free layer exists. It carries counterflow of the normal and superfluid components and separates the vortex array from the container wall. In addition to MV's, a small number of SMV's exists. These are topologically bound to planar defects,[11] so-called $\theta$ solitons.[12] It follows that the SMV's either appear as bound pairs or are attached to the wall of the experimental cell by the soliton. Both these structures are stabilized by the Magnus forces acting on the MV parts of the SMV's. The presence of solitons explains both the frequency shifted absorption in the NMR spectrum and the increased HPD absorption; the two configurations of SMV's are needed to explain the measured dependence of the additional HPD absorption on rotation velocity.

The most consistent method to create the state showing evidence of SMV's is to let the sample undergo a transition from the $A$ to the $B$ phase during rotation under thermodynamically reversible conditions. A state with a strongly deformed conventional NMR spectrum is observed right after the transition. The initial state, which evidently contains a large number of SMV's, decays in several minutes to a more stable structure which contains from one up to several tens of SMV's. The final state is only barely distinguishable in the conventional NMR spectrum, but the solitons are clearly revealed by

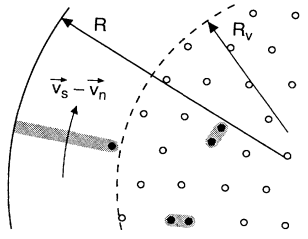


FIG. 1. Schematic cross section of the cylindrical experimental cell (radius = $R$) rotating around its axis. The number of mass vortices (open circles) is less than in equilibrium and, consequently, there is a vortex-free layer that carries macroscopic counterflow of the normal and superfluid components at velocity $\mathbf{v}_s - \mathbf{v}_n$. In addition, there are $\theta$ solitons (grey) emerging from spin-mass vortices, SMV's (solid circles) in two configurations: a pair of SMV's bound together by the $\theta$ soliton or a single SMV with the soliton attached to the cell wall.

 

the large additional HPD absorption, still present, although to a lesser extent than in the initial state.

We start in Sec. II with a discussion of different planar and linear defects in $^3$He-$B$. The two modes of NMR are introduced in Secs. III and IV and our experimental cell is described in Sec. V. In Sec. VI we discuss the nonequilibrium situations, under which the SMV's were observed to nucleate. The conventional NMR spectrum is explained in Sec. VII. The HPD absorption measurements are described in Secs. VIII and IX; the positional stability of the SMV is studied in Sec. VIII B. A short summary is given in Sec. X. The main findings have been reported in Ref. 13.

## II. PLANAR AND LINEAR DEFECTS IN $^3$He-$B$

### A. Bulk superfluid

Superfluid states can be analyzed according to principles applicable to any system of broken symmetry.[14] For normal helium, either $^4$He or $^3$He, the symmetry group can be written as

$$G = \mathrm{U}(1) \times \mathrm{SO}_3^{(S)} \times \mathrm{SO}_3^{(L)} \quad . \tag{1}$$

Here U(1) is the gauge group, which is equivalent to its representation by the phase factor $e^{i\Phi}$. $\mathrm{SO}_3^{(S)}$ and $\mathrm{SO}_3^{(L)}$ denote the group of (three-dimensional) rotations in spin and orbital spaces, respectively. Superfluidity is characterized by broken gauge symmetry U(1), which is the only broken symmetry in superfluid $^4$He. Therefore, the order parameter of $^4$He is a complex scalar $A = \Delta e^{i\Phi}$, where $\Delta$ is real. The state is degenerate with respect to the phase $\Phi$. This allows only one type of topologically stable defect, the usual mass vortex (MV), for which $\Phi$ changes by $2\pi$ while encircling the vortex line.

Superfluid $^3$He has a more complicated structure than $^4$He. The superfluid phases belong to a representation of $G$ that can be described by a $3\times3$ matrix order parameter $A_{\alpha j}$.[15] Here $\alpha$ and $j$ are indices in spin and orbital spaces, respectively. The different superfluid phases of $^3$He are distinguished by their remaining symmetry.

The simplest equilibrium state of the $B$ phase, which can be chosen as an initial state, is[15]

$$A^{(0)}_{\alpha i} = \Delta_B \, \delta_{\alpha i} \quad . \tag{2}$$

If $\underline{R}^{(1)}$ and $\underline{R}^{(2)}$ are matrices of spin and orbital rotations, respectively, and $e^{i\Phi}$ is the operation of the gauge transformation, then the $B$-phase state $A^{(0)}_{\alpha i}$ transforms under operations of the symmetry $G$ into another degenerate $B$-phase state described by the order parameter

$$A_{\alpha i} = e^{i\Phi} R^{(1)}_{\alpha\beta} R^{(2)}_{ik} A^{(0)}_{\beta k} = \Delta_B \, e^{i\Phi} R_{\alpha i} \quad , \tag{3}$$

where the conventional $\underline{R}$ matrix of the $B$ phase is expressed in terms of $\underline{R}^{(1)}$ and $\underline{R}^{(2)}$ as

$$\underline{R} = \underline{R}^{(1)} (\underline{R}^{(2)})^{-1} \quad . \tag{4}$$

Only relative spin and orbital rotations lead to a new equilibrium state, while the combined rotations with $\underline{R}^{(1)} = \underline{R}^{(2)}$ leave the state unchanged. Therefore, the space of the degenerate states of the $B$ phase includes the circumference U(1) of the phase $\Phi$ and the $\mathrm{SO}_3^{(S-L)}$ space of the $\underline{R}$ matrix:

$$\mathrm{U}(1) \times \mathrm{SO}_3^{(S-L)} \quad . \tag{5}$$

The orthogonal matrix $R_{\alpha j}(\hat{\mathbf{n}}, \theta)$ can be parametrized by an axis $\hat{\mathbf{n}}$ and an angle $\theta$ of rotation: $R_{\alpha i}(\hat{\mathbf{n}}, \theta) = \cos\theta \delta_{\alpha i} + (1 - \cos\theta)\hat{n}_\alpha \hat{n}_i - e_{\alpha ik}\hat{n}_k \sin\theta$.

In the foregoing we have neglected a small spin-orbit coupling caused by the magnetic dipole-dipole interaction of the $^3$He nuclei, which is described by the energy

$$F_D = \tfrac{8}{5} g_D (\cos\theta + \tfrac{1}{4})^2 \quad . \tag{6}$$

The coefficient $g_D = \frac{1}{3}\chi_B \Omega_L^2/\gamma^2$, where $\Omega_L$ is the longitudinal resonance frequency, $\chi_B$ is the susceptibility, and $\gamma$ is the absolute value of the negative gyromagnetic ratio for the $^3$He nucleus. The spin-orbit coupling lifts the degeneracy $\mathrm{SO}_3^{(S-L)}$ slightly by favoring for $\theta$ the value $\theta_L = \arccos(-\frac{1}{4}) \approx 104°$, but it leaves $\hat{\mathbf{n}}$ arbitrary. The remaining degeneracy, due to the unit vector $\hat{\mathbf{n}}$, is lifted by an external magnetic field, the superfluid vs normal liquid counterflow $\mathbf{v}_s - \mathbf{v}_n$, and the walls of the experimental chamber:

$$F_H = -\frac{a}{\chi_B^2} (\hat{\mathbf{n}} \cdot \mathbf{M})^2, \tag{7a}$$

$$F_{\mathrm{cf}} = -\frac{g_{\mathrm{cf}}}{\chi_B^2} [M_\alpha R_{\alpha i} (\mathbf{v}_s - \mathbf{v}_n)_i]^2, \tag{7b}$$

$$F_{\mathrm{surf}} = -\frac{d}{\chi_B^2} [M_\alpha R_{\alpha i} \hat{w}_i]^2 \quad , \tag{7c}$$

where $\hat{\mathbf{w}}$ is the normal to the vessel wall and $\mathbf{M}$ is the magnetization, equal to $\chi_B \mathbf{H}$ in equilibrium. For example, the magnetic energy $F_H$ is minimized when $\pm\hat{\mathbf{n}}$ is along the magnetic field $\mathbf{H}$.

Bending the order-parameter field induces a gradient energy

$$F_\nabla = \frac{\chi_B c^2}{8\gamma^2} [\partial_i R_{\alpha j} \partial_i R_{\alpha j} + 2(\partial_i R_{\alpha i})^2] \quad , \tag{8}$$

where $c$ is the transverse spin-wave velocity. Therefore, continuous configurations, called textures, are formed with a smoothly varying order parameter. The healing length, over which the texture relaxes to that of the undisturbed state, is determined by the strength of the orienting interaction and the gradient energy density. Usually the superfluid condensation energy is the dominant term. It drives the order parameter to its bulk form (3) within a distance of the coherence length $\xi \sim 0.01$–$0.1\,\mu$m from a strong perturbation, such as a wall. The dipole energy (6) is much smaller than the superfluid condensation energy. Thus $\theta$ relaxes to its bulk value $\theta_L$ on a longer length scale $\xi_D \approx 10\,\mu$m. Finally, the healing lengths for $\hat{\mathbf{n}}$ are longer than $\xi_D$ because the orienting

energies (7) are smaller than the dipole energy. For example, if $\hat{\mathbf{n}}$ is distorted from the direction $\pm\mathbf{H}$ at some location, it approaches its equilibrium direction on the scale of the magnetic healing length $\xi_H$, which is approximately 1 mm in a field of 10 mT. So the ratios of the characteristic lengths are $\xi : \xi_D : \xi_H \sim 1 : 10^2 : 10^4$.

### B. Solitons

The topology of planar defects, or solitons, in $^3$He-$B$ has been worked out by Mineev and Volovik.[11] Because there is no planar defect corresponding to U(1), we can restrict the discussion to the $SO_3^{(S-L)}$ degeneracy parametrized by $\hat{\mathbf{n}}$ and $\theta$. This parameter space can be represented graphically as a solid sphere of the vector $\theta\hat{\mathbf{n}}$, see Fig. 2. The radius of the sphere is $\pi$, and diametrically opposite points on the surface are identified, since rotations by $\pi$ around $\hat{\mathbf{n}}$ and $-\hat{\mathbf{n}}$ lead to the same final state. In this representation, rotation by an angle $\theta > \pi$ around $\hat{\mathbf{n}}$ is considered a rotation by $2\pi - \theta$ around the axis $-\hat{\mathbf{n}}$. The dipole forces favor a spherical surface $S^2$ of radius $\theta_L$ within the solid sphere, while the orienting energies for $\hat{\mathbf{n}}$ favor some particular points on $S^2$.

A point $\mathbf{r}$ in the real space can be mapped to a point $\theta(\mathbf{r})\hat{\mathbf{n}}(\mathbf{r})$ in the order parameter space $SO_3^{(S-L)}$. A line, which is drawn through a planar defect in real space, corresponds to a path $\Gamma$ in $SO_3^{(S-L)}$. As the end points of $\Gamma$ mark the order parameter far from the defect, they must be energy minima and lie on $S^2$. All the possible $\Gamma$'s can be composed of paths which are topologically equivalent to two types of solitons: an $\hat{\mathbf{n}}$ soliton and a $\theta$ soliton. The $\hat{\mathbf{n}}$ soliton corresponds to a path lying on $S^2$ while the path representing the $\theta$ soliton cannot be transformed continuously to a path on $S^2$.

An example of an $\hat{\mathbf{n}}$ soliton in a magnetic field is shown in Fig. 2(a).[16] The magnetic energy is minimized when $\hat{\mathbf{n}}$ is parallel to $\pm\mathbf{H}$ and, therefore, a soliton is formed when $\hat{\mathbf{n}}$ turns from the direction $+\mathbf{H}$ to $-\mathbf{H}$. In this soliton, $\theta$ remains equal to $\theta_L$, so that the minimum of the dipole energy is achieved everywhere. Because only the magnetic orienting energy is lost in the soliton, it has approximately the thickness $\xi_H$. Another type of $\hat{\mathbf{n}}$ soliton can appear in a long cylindrical cell where there are more than one degenerate axial texture due to the boundary conditions and the interaction with the superflow, and these may be stacked in the cell above each other. $\hat{\mathbf{n}}$ solitons have been observed in NMR cells with a slab[17] or cylindrical[18,19] geometry. They are frequently formed in a cylindrical chamber during rapid cooling, and disappear if the texture is annealed by large counterflow between the normal and superfluid components.[19]

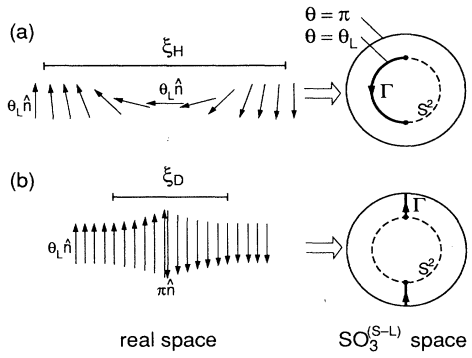


FIG. 2. Schematic illustration (a) of an $\hat{\mathbf{n}}$ soliton and (b) of a $\theta$ soliton. On the left, the vector $\theta\hat{\mathbf{n}}$ is depicted as a function of the coordinate perpendicular to these planar defects. On the right, the space $SO_3$ of matrix $R_{\alpha i}(\hat{\mathbf{n}}, \theta)$ is represented as a solid sphere of $\theta\hat{\mathbf{n}}$. The radius of the sphere is $\pi$ and two diametrically opposite points $\pi\hat{\mathbf{n}}$ and $-\pi\hat{\mathbf{n}}$ are identified. The dipole-dipole interaction favors the surface $\theta = \theta_L \approx 104°$. The two solitons correspond just to the two topologically nonequivalent paths $\Gamma$ in $SO_3$.

In a $\theta$ soliton the rotation angle goes once (or an odd number of times) through $\pi$. The most economic structure is obtained if $\theta$ increases from $\theta_L$ to $2\pi - \theta_L$, while $\hat{\mathbf{n}}$ remains constant. In terms of $\theta$ angles limited between 0 and $\pi$, the $\theta$ angle within this soliton first increases from $\theta_L$ to $\pi$ and then decreases from $\pi$ to $\theta_L$, but with opposite direction of $\hat{\mathbf{n}}$, see Fig. 2(b). Because the dipole energy is not minimized in the $\theta$ soliton, its thickness is on the order of the dipole length $\xi_D$. The order parameter within the soliton has been calculated in Ref. 12. The lowest energy is achieved when $\hat{\mathbf{n}}$ is perpendicular to the plane of the soliton. Topologically, $\theta$ solitons obey the summation law $1 + 1 = 0$ because a path going twice through $\pi$ can be contracted to a path lying wholly on $S^2$.[15]

### C. Vortices

From the topological point of view, line defects of the $B$ phase are described by two integer quantum numbers, $\nu$ and $\nu_R$. These correspond to the two constituents of the first homotopy group of the order-parameter space in the $B$ phase:[20,21]

$$\pi_1[\mathrm{U}(1) \times SO_3^{(S-L)}] = Z \times Z_2 \quad . \tag{9}$$

Here $\nu$ belongs to the group $Z$ of integers, while the group $Z_2$ contains only two elements: $\nu_R = 0$ and $\nu_R = 1$ with the summation rule $1 + 1 = 0$. When a line with $\nu \neq 0$ and $\nu_R = 0$ is encircled once, the overall phase $\Phi$ of the order parameter changes by $2\nu\pi$. This leads to azimuthal superfluid velocity

$$\mathbf{v}_s = \frac{\hbar}{2m_3}\nabla\Phi = \nu\frac{\kappa}{2\pi r}\hat{\boldsymbol{\phi}} \quad , \tag{10}$$

around the line, i.e., it is a conventional quantized vortex with $\nu$ quanta of circulation $\kappa = h/2m_3$ of $\mathbf{v}_s$. We call this structure the mass vortex (MV) because of the flow $\mathbf{j} = \rho_s\mathbf{v}_s$ around the line; here $\rho_s$ is the superfluid density. In the vortex core, the order parameter deviates from its bulk form (3), and Eq. (10) is not valid. The core has the characteristic size of $\xi$. Two types of singly quantized MV's with different core structures have been

found experimentally [1] and theoretically [2] to be stable in the $B$ phase: The MV at high pressures and high temperatures is axially symmetric while the low-temperature vortex has an asymmetric double core.

The other type of line defect is characterized by the quantum numbers $\nu = 0$ and $\nu_R = 1$. In this defect there is no change of phase but, in the simplest representation, the angle $\theta$ in the rotation matrix $R_{\alpha j}(\hat{\mathbf{n}}, \theta)$ changes by $2\pi$ while encircling the line once. Because $R_{\alpha j}$ is related to the direction of the spin, its spatial changes lead to flow of spin, i.e., spin currents.[22] Therefore, we call this object a spin vortex (SV). The structure of an SV depends on the distance from the line in a more complicated way than that of an MV: starting from the smallest, there is a "hard" core of characteristic size $\xi$, where the order parameter deviates from the $B$-phase form (3). At distances $\xi < r < \xi_D$ the SV is approximately described by Eq. (3), where $\Phi$ and $\hat{\mathbf{n}}$ are nearly constant but $\theta$ is roughly equal to the azimuthal angle around the line.[23,24] There is nearly axially symmetric spin flow around the SV at these distances. When $r > \xi_D$, the nearly axial structure is broken. The dipole-dipole interaction tries to make $\theta$ equal to $\theta_L$. This is accomplished in most of the liquid but, by topology, there necessarily remains a $\theta$ soliton that emerges from the SV line[20] (see Fig. 3). A path around the SV is mapped on a closed contour $\Gamma_1$ in $SO_3^{(S-L)}$. The path $\Gamma_1$ penetrates once the surface $\theta = \pi$, which makes it noncontractable. If two paths $\Gamma_1$ are joined, the resulting contour can be contracted to a point. Thus two SV's can annihilate each other.

We emphasize that the attachment of a planar defect to a line is a general consequence of lifting the degeneracy on which the line defect is based. A topological bond of the same kind occurs in liquid crystals [25] and in some theories of high-energy physics,[26] where walls terminating on strings and strings terminating on monopoles are discussed. In the case of $^3$He-$B$, the existence of the SV is based on the approximate degeneracy $SO_3^{(S-L)}$, and a small lifting of this degeneracy gives rise to the $\theta$ soliton attached to the SV.

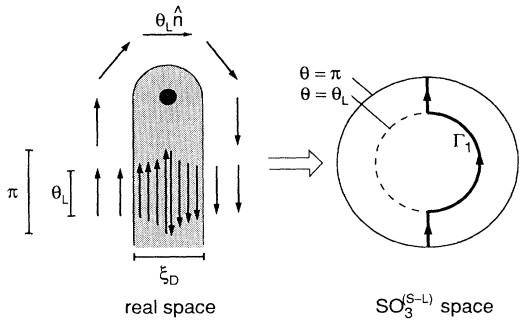


FIG. 3. Schematic illustration (left) of a spin or a spin-mass vortex, which consist of a linear core (black dot) and a planar $\theta$ soliton tail (grey). The arrows denote the vector $\theta\hat{\mathbf{n}}$ on a path encircling the vortex line. This path is mapped (at right) on a noncontractable closed contour $\Gamma_1$ in the $SO_3$ space. In a real case, the arrows should be rotated by 90° in the plane of the paper, because the minimum energy is obtained when $\hat{\mathbf{n}}$ is perpendicular to the plane of the soliton.

Although the SV is topologically stable, it is expected to exist only under special circumstances. An example is a restricted geometry with a characteristic length of about $\xi_D$ or smaller, so that the dipole-dipole forces are not important. In the bulk liquid, the SV is bound to the soliton tail, which has surface tension trying to reduce its area. Therefore, the SV can be stable in the bulk liquid only if it is pinned so that the surface tension is compensated.

A suitable object, which can trap the disclination line, is the usual mass vortex. If a spin and a mass vortex are combined, a third possible type of linear defect in $^3$He-$B$, a spin-mass vortex (SMV), is formed with quantum numbers $\nu = 1$ and $\nu_R = 1$. There is no energy term below order $v_s^2 v_{\rm spin}^2$ that gives coupling between the $\Phi$ field of the MV and the $\theta$ field of the SV. Thus appreciable interaction between the MV and the SV takes place only when their hard cores overlap. Because superfluid condensation is reduced in the hard cores of the vortices, it is energetically favorable to unite the MV and SV so that a common hard core is formed. In fact, a more detailed analysis reveals that the energy gain is much larger than predicted by this simple argument.[23] It follows that, in order to separate the SV part from a MV line, the system needs to overcome a potential barrier and, as a result, the SMV may exist as a metastable state. The core structures of MV's and SMV's have been studied in Ref. 27 in a particularly simple limiting case.

## III. CONVENTIONAL NMR TECHNIQUE

Conventional NMR at low rf excitation levels can be used for studying the texture in $^3$He-$B$. Information is obtained from the frequency shifts in the absorption spectrum. In the high-field limit, the shift of the resonance frequency $\omega$ from the Larmor value $\omega_0 = \gamma H$ is given as $\omega - \omega_0 = [\Omega_L^2/(2\omega_0)] \sin^2\psi$, where $\psi$ is the angle between the polarizing field $\mathbf{H}$ and the anisotropy axis $\hat{\mathbf{n}}$. When $\hat{\mathbf{n}}$ varies in space, this result can be applied locally at every point, provided that the variation is small on the scale of $\xi_D$. Therefore, the spectrum directly gives the distribution of $\sin^2\psi$ in the experimental cell. In a long cylinder, whose axis is parallel to $\mathbf{H}$, the $\hat{\mathbf{n}}$ texture has the flare-out structure:[19,28] $\hat{\mathbf{n}}$ is parallel to $\mathbf{H}$ along the axis of the cylinder and heals smoothly to an angle $\psi \approx \arcsin(2/\sqrt{5}) \approx 63°$ at the walls which corresponds to the minimum of the surface energy $F_{\rm surf}$ in Eq. (7). The corresponding NMR spectrum contains an absorption maximum, which borders to the Larmor frequency and originates from the central region of the cell, and a tail, which extends to the normalized frequency shift $\sin^2\psi = (2\omega_0/\Omega_L^2)(\omega - \omega_0) = \frac{4}{5}$.

All the planar and linear defects, which were discussed in Sec. II, disturb the $\hat{\mathbf{n}}$ texture and can, in principle, be detected by conventional NMR measurements. Under typical experimental conditions, $\xi_H$ is much longer than the intervortex distance. Therefore, MV's have an averaged effect on the $\hat{\mathbf{n}}$ texture. In spite of this, detailed information has been extracted about MV's by studying

the textures with conventional NMR, which reveals, for example, the phase transition between the two MV's and the ferromagnetic properties of the vortex cores.[1] The $\hat{\mathbf{n}}$ solitons are clearly displayed if they are such that $\hat{\mathbf{n}}$ turns perpendicular to $\mathbf{H}$ inside the soliton. This orientation of $\hat{\mathbf{n}}$ produces a peak in the NMR spectra at the maximum frequency shift $\sin^2\psi = 1$. A similar peak is seen in the present experiment, where it is believed to be induced by $\hat{\mathbf{n}}$ textures associated with $\theta$ solitons. The volume of the solitons may be too small to become directly visible in a conventional NMR experiment.

## IV. COHERENT SPIN PRECESSION

There exists a resonance mode which is peculiar to $^3$He-$B$. In this mode, called the homogeneously precessing domain, HPD,[5–7] the stationary $\hat{\mathbf{n}}$ texture is obliterated. Instead, $\hat{\mathbf{n}}$ tends to precess uniformly, which means that, compared to the conventional NMR, quite different information about the defects in $^3$He-$B$ can be obtained. The resonance absorption in the HPD includes contributions directly from inhomogeneities like vortex cores and $\theta$ solitons. Essential new knowledge about MV's has been obtained with this technique. For example, the asymmetry of the vortex core in the low-temperature MV has been resolved: the Goldstone mode associated with oscillations in the spontaneous anisotropy of the vortex core has been excited and detected.[10] Here it will be shown that $\theta$ solitons produce in the HPD large additional resonance absorption, which is a more prominent characteristic of $\theta$ solitons than their signature in the conventional NMR spectrum.

### A. Bulk HPD

In the HPD the magnetization $\mathbf{M}$ precesses coherently around $\mathbf{H} = H\hat{\mathbf{z}}$ with a tipping angle near $\theta_L = 104°$. This angle is unique for the following reason. A necessary condition for solutions that precess uniformly at the Larmor frequency $\omega_0 = \gamma H$ is

$$M_\alpha = \chi_B R_{\alpha\beta} H_\beta \ . \tag{11}$$

This equation follows from the Leggett equations,[29] but it also can be proved by symmetry arguments (see Appendix). Equation (11) says that the magnitude of the precessing magnetization is equal to its equilibrium value, and $\underline{R}(\hat{\mathbf{n}},\theta)$ maps the field into the direction of the magnetization. When the tipping angle of $\mathbf{M}$ is smaller than $\theta_L$, the minimum of the dipole energy (6) can be satisfied simultaneously with Eq. (11). The precession frequency $\omega = -\gamma(\partial F/\partial M_z)$ is then equal to $\omega_0$ because only the Zeeman energy $-\mathbf{M}\cdot\mathbf{H}$ contributes to $F$. At larger tipping angles the dipole energy starts to increase. This gives rise to a shift of frequency from the Larmor value. In order to satisfy (11) in the HPD, $\hat{\mathbf{n}}$ is perpendicular to both $\mathbf{H}$ and $\mathbf{M}$, and $\mathbf{M}\cdot\mathbf{H} = \cos\theta$, as shown in Fig. 4 in the region outside of the soliton.

In contrast to the HPD, the equilibrium state is called

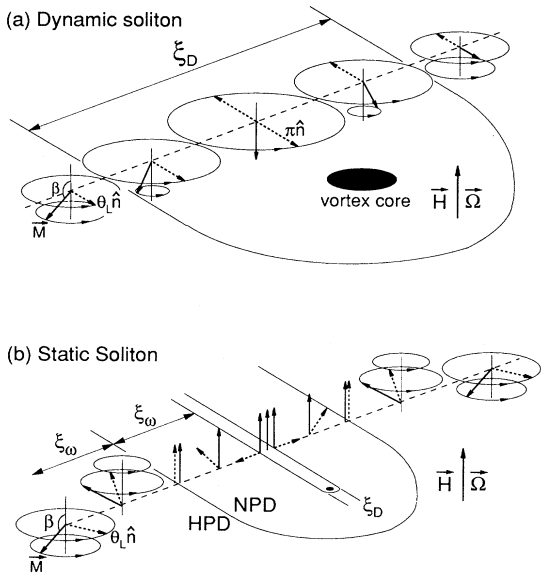


FIG. 4. Two ways in which the $\theta$ soliton can be imagined to coexist with the HPD. Dashed arrows depict $\theta\hat{\mathbf{n}}$, while solid arrows show magnetization $\mathbf{M}$. In (a) $\hat{\mathbf{n}}$ precesses everywhere in the plane perpendicular to $\mathbf{H}$ so that $\hat{M}_\alpha = R_{\alpha j}(\hat{\mathbf{n}},\theta)\hat{H}_j$. The tipping angle $\beta$ of $\mathbf{M}$ equals $\theta$ and is 180° in the middle of the soliton, where the precession phase of the spins turns by 180°. In (b) the soliton has a static structure with $\hat{\mathbf{n}}$ perpendicular to the soliton wall and $\mathbf{M} \uparrow\uparrow \mathbf{H}$. The bulk HPD is separated from the soliton by two regions of widths $\xi_\omega$. The inner of these is a sheet of nonprecessing domain where $\hat{\mathbf{n}}$ turns parallel to $\mathbf{H}$, while in the outer, $\mathbf{M}$ tilts to the orientation $\beta = \theta \approx \theta_L$ of the bulk HPD.

the nonprecessing domain (NPD). There the magnetization $\mathbf{M} = \chi_B\mathbf{H}$, and the structure of $\underline{R}(\hat{\mathbf{n}},\theta)$ was discussed in Sec. II.

As long as the energy dissipation is small, the precessing states can be analyzed in terms of energy functionals. In cw-NMR experiments there is an rf field that precesses at some frequency $\omega$ ($\boldsymbol{\omega} \parallel \mathbf{H}$). Because it is the frequency rather than the total magnetization that is specified, a term $\boldsymbol{\omega}\cdot\mathbf{M}/\gamma$ has to be combined with the Zeeman energy:

$$F_\omega = \left(\frac{\omega}{\gamma H} - 1\right)\mathbf{M}\cdot\mathbf{H}. \tag{12}$$

Minimization of this energy implies that the NPD is favored for $H > \omega/\gamma$, whereas the HPD has lower energy in smaller fields. In the HPD, tipping angles larger than $\theta_L$ are opposed by the dipole energy (6). Because $F_D$ usually is much larger than $F_\omega$, the tipping angle is only slightly larger than $\theta_L$. In other words, the difference $\omega - \gamma H$ is compensated by the dipolar frequency shift without an appreciable change of the tipping angle.

The effective Zeeman energy (12) determines, together with the gradient energy (8), a characteristic dynamical healing length $\xi_\omega = c/\sqrt{\omega(\omega - \gamma H)}$.

It should be noted that, besides the vortices and solitons mentioned in Secs. II B and II C, there exist funda-

mentally different types of topological objects in $^3$He-$B$, which can arise in the presence of the coherent spin precession, since the precessing states have their own space of degeneracy.[30] An example of such objects is the dynamical spin vortex,[31] in which the phase of the precessing magnetization changes by $2\pi$ while encircling the line. On approaching the vortex line, the magnetization turns parallel to the field. In this way the order parameter can retain everywhere the $B$-phase form (3). The core size of this vortex is on the order of $\xi_\omega$.

### B. Two-domain structure

The HPD and NPD can exist simultaneously if a field gradient $\nabla H$ is applied.[5,6] A domain boundary between the HPD and the NPD is then formed at the position where $H = \omega/\gamma$. The HPD fills the region where $\gamma H < \omega$ and the NPD the remaining region with $\gamma H > \omega$. When crossing the domain boundary, the precessing $\hat{\mathbf{n}}$ vector is reoriented from the plane $\hat{\mathbf{n}} \perp \mathbf{H}$ well inside the HPD region to $\hat{\mathbf{n}} \parallel \mathbf{H}$ in the NPD. Correspondingly, the tilting angle of magnetization changes from $\theta_L$ on the HPD side to zero on the NPD side of the domain boundary. The characteristic thickness $\lambda_0$ of the boundary is obtained by comparison of the effective Zeeman energy (12) $\sim \chi_B H \nabla H \lambda$ with the gradient energy (8) $\sim \chi_B c^2/\gamma^2\lambda^2$, which gives $\lambda_0 \sim (c^2/\omega\gamma\nabla H)^{1/3}$ [6]. (Depending on the context, $\nabla H$ is either a vector or the magnitude of the field gradient.) For some reason (see below), the HPD–NPD boundary may be forced out of its free equilibrium position. Then the characteristic thickness of the boundary is the smaller one of the lengths $\lambda_0$ and $\xi_\omega$.[32]

The constant field gradient $\nabla H$ is parallel to $\mathbf{H}$ in our experiments. Therefore the domain boundary is perpendicular to $\mathbf{H}$. $\nabla H$ is kept constant ($\sim$ 5 mT/m). In generating the HPD, $H$ ($\sim$ 10 mT) is swept down from some value at which $H(z) = H(0) - z\nabla H$ is larger than $\omega/\gamma$ throughout the cell. Here $z$ is the vertical position in the cell in the direction of $\nabla H$, counted from the bottom. When $H(z = L)$ is reduced below $\omega/\gamma$, an HPD of length $\tilde{L} = L - z_0$ is formed; here $z_0$ is defined by the condition $\omega = \gamma H(z_0)$. By sweeping the magnitude of $H$, the domain boundary can be moved across the volume of the $^3$He-$B$ liquid.

Owing to the dipole torque acting on the precessing spins within the HPD, the Leggett-Takagi relaxation of spins takes place.[33] In addition, relaxation caused by spin diffusion occurs within the boundary, where the magnetization is inhomogeneous. The energy dissipation in the precessing domain and within the boundary is compensated by the power absorbed to the spin system from the rf field [we apply $H_{\rm rf}(\omega t) \sim 10^{-4}$ mT]. The HPD is stable as long as the rf field can supply enough power. The resonance absorption attains an additional contribution in the presence of other inhomogeneities, such as quantized vortices and $\theta$ solitons.

### C. $\theta$ soliton within the HPD

We consider two possible ways in which the $\theta$ soliton can coexist with the HPD. We restrict the discussion to the case when $\mathbf{H}$ is in the plane of the soliton.

*Dynamic soliton.* In this structure, the HPD completely penetrates into the soliton, see Fig. 4(a). As a first approximation, $\underline{R}$ has the same structure as in the equilibrium soliton (Fig. 3) except that $\hat{\mathbf{n}}$ precesses everywhere around $\mathbf{H}$. The magnetization $\mathbf{M}$ is given by Eq. (11), i.e., the tipping angle of $\mathbf{M}$ changes in the soliton from the bulk value $\theta_L$ to $\pi$ and then back to $\theta_L$ but with the phase of the precession of $\mathbf{M}$ changed by $\pi$, because $\hat{\mathbf{n}}$ has opposite directions on the opposite sides of the soliton. In a quantitative analysis one should take into account that both the $\underline{R}$ and $\mathbf{M}$ fields are distorted by spin diffusion and the rf field, but the topological structure of the soliton remains unchanged. The most economical structure is not achieved because the precessing $\hat{\mathbf{n}}$ can only momentarily be normal to the soliton wall. This gives rise to an extra energy on the order of the dipole-dipole energy (6) times $\xi_D$.

*Static soliton.* The second alternative is that the HPD does not penetrate into the soliton. The soliton becomes covered by the HPD-NPD interface with a thickness of the order of $\xi_\omega$, see Fig. 4(b). The soliton core is time independent: $\underline{R}$ preserves the equilibrium configuration and $\mathbf{M} = \chi_B\mathbf{H}$. Starting from the soliton wall, $\hat{\mathbf{n}}$ reorients from the direction normal to the soliton wall to $\hat{\mathbf{n}} \| \mathbf{H}$ at the NPD-HPD interface. On the HPD side of the interface, the precessing $\hat{\mathbf{n}}$ vector changes from $\hat{\mathbf{n}} \| \mathbf{H}$ to the bulk orientation $\hat{\mathbf{n}} \perp \mathbf{H}$. The orientation $\hat{\mathbf{n}} \| \hat{\mathbf{z}}$ at the interface is the only possibility to match the precessing and nonprecessing $\hat{\mathbf{n}}$ in the case $\sqrt{\gamma H(\omega - \gamma H)} << \Omega_L$,[30] corresponding to our conditions. This structure has lower energy than the dynamic soliton because the soliton core can attain its minimum energy and the energy cost of the HPD-NPD interface is smaller than the extra energy of the soliton core by the factor of $\xi_D/\xi_\omega$.

The solitons are observable in an NMR experiment because of the absorption caused by spin diffusion in an inhomogeneous magnetization. The two possible structures have different NMR signatures: The magnetization of a static soliton is inhomogeneous within the $\hat{\mathbf{n}}$ texture on the HPD side of the HPD-NPD interface. This inhomogeneity, and the spin-diffusion relaxation, depends on $\omega - \gamma H(z)$. In a dynamic soliton, the inhomogeneity of the magnetization is concentrated to the soliton core of width $\sim \xi_D$. Consequently, the absorption should not depend on $\omega - \gamma H(z)$.

## V. EXPERIMENTAL TECHNIQUES

Our experiments were done in the rotating nuclear demagnetization cryostat ROTA1.[34] The NMR cell, shown in Fig. 5, is the same that was used in the measurements of Refs. 4, 9, and 10: a cylinder of radius $R$ = 3.5 mm, height $L$ = 7 mm, and the symmetry axis aligned along the axis of rotation. The cell is separated from the main part of the $^3$He volume, housing the sintered heat exchanger and the platinum NMR thermometer coil, by means of an orifice (diameter = 1.0 mm, height = 0.5 mm) and a channel (diameter = 1.5 mm, length = 5.5 mm).

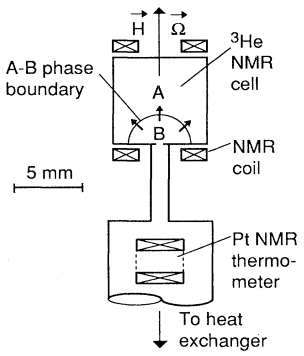


FIG. 5. Cross section of the $^3$He chamber during an $A \rightarrow B$ transition.

This construction was selected for two reasons. Firstly, it is convenient in the HPD measurement because experiments can then be performed with a well-defined precessing domain which is nearly detached from the rest of the $^3$He. Secondly, our cell construction is essential if one wants to achieve a rotating vortex-free state with large superfluid vs normal liquid counterflow. The channel and the orifice block the leakage of vortices from the heat exchanger volume to the NMR cell. Because of its large diameter (30 mm) and porous material, the heat exchanger enhances vortex nucleation and can trap remnant vorticity. In earlier experiments,[19] in which the heat exchanger volume was nearly identical to ours but open without a constriction to the NMR cell, vortices started to form at $\Omega < 0.2$ rad/s. In the present NMR cell, the critical rotation velocity $\Omega_c$ for the nucleation of vortices is high, in $^3$He-$B$, $\Omega_c > 2.8$ rad/s at $T > 0.6T_c$ and at 29.3 bar pressure.

The minimum energy configuration in the rotating $B$ phase is a lattice of singly quantized vortices with a density $n = 2\Omega/\kappa$, where $\kappa = h/2m_3$ is the quantum of circulation. Because of the high $\Omega_c$, a state can be prepared in which there is only a fraction of the vortices that would be present in equilibrium, $N_{\rm eq} = \pi R^2 n$. In this state the vortices form a cluster in the center of the cell, having the equilibrium vortex density and a radius $R_v = R\sqrt{\Omega_V/\Omega}$; $\Omega_V$ is the rotation velocity corresponding to the number of vortices, $N = \pi R_v^2 n = \pi R^2(2\Omega_V/\kappa)$, in the cluster. This state can be observed by conventional NMR because the macroscopic counterflow $\mathbf{v}_s - \mathbf{v}_n$ in the annular vortex-free region (see Fig. 1) around the cluster orients the texture.[4,19,3] When the counterflow velocity exceeds the so-called dipolar velocity $v_D$, its effect, $F_{\rm cf}$ in Eq. (7), becomes larger than that of the magnetic orientational energy $F_H$, which tries to align $\hat{\mathbf{n}} \parallel \mathbf{H}$.[3] In our cell, a difference $\Omega - \Omega_V \approx 0.3$ rad/s leads to the appearance of a plateau in the $\psi(r)$ distribution, and a counterflow absorption maximum is observed in the conventional NMR spectrum near $\sin^2\psi = 0.8$, which corresponds to the minimum of $F_{\rm cf}$.[4] The frequency shift and the intensity of the counterflow peak can be used to determine the number of vortices in the cluster with a resolution of 10 vortices in the best cases.

The temperature of the sample was determined (i) with a pulsed Pt-NMR thermometer, (ii) by measuring the magnetization $M(T) = \chi_B(T)H$ of the sample in the HPD resonance mode, or (iii) from the longitudinal resonance frequency extracted from the conventional NMR spectrum. The experiments were performed at 29.3 bar pressure in a magnetic field of 28.4 or 14.2 mT.

## VI. CREATION OF SPIN-MASS VORTICES

The anomalous state showing evidence of SMV's is formed in a few nonequilibrium situations. One of these occurs when the $^3$He sample is cooled from the $A$ to the $B$ phase during rotation at constant $\Omega$. In $^3$He-$A$, vortices can be detected using NMR;[1] in our cell we always observed doubly quantized continuous vortices. These are nucleated already at $\Omega < 0.2$ rad/s and the equilibrium rotating state is easily obtained. A continuous $A$-phase vortex cannot penetrate through the $AB$ interface as such: its vorticity is distributed to the large soft core of size $\xi_D$, and in the $B$ phase it must be concentrated to the hard core of size $\xi$.[35–37] This means a reduction of roughly $10^{-5}$ in the area. The rotation velocity during the transition, $\Omega_{AB}$, was in our experiments selected smaller than $\Omega_c$, which means that $B$-phase vortices were not nucleated at the walls after the $A \rightarrow B$ transition.

In our experiments, the amount and type of vortices nucleated during the $A \rightarrow B$ transition depended both on $\Omega_{AB}$ and the duration of the transition $t_{AB}$. After a hypercooled transition at $T \approx 0.8T_{AB}$, where $T_{AB} = 0.85T_c$ is the thermodynamic transition temperature at $p = 29.3$ bars,[38] the usual $B$-phase state was found, with an equilibrium number of MV's. The hypercooled transition takes place in about 10 ms,[39] so rapidly that the circulation and the angular momentum cannot be removed from $^3$He-$A$, in which the time scale for the mutual-friction-resisted vortex motion is 1–10 s.[40]

Following a reversible $A \rightarrow B$ transition with $t_{AB}$ larger than about 1 s and $\Omega_{AB} > 0.3$ rad/s, an anomalous state was formed which contained, as it will be shown later, both MV's and SMV's, but in which the total vortex number was less than in equilibrium. After the transition, the total vortex number remained constant, but some SMV's may have lost their disclinations and turned to MV's before stable conditions were reached.

Systematic studies of how the number of MV's depends on the transition time and on $\Omega_{AB}$ will be presented elsewhere.[35] These experiments show that the presence of the $AB$ interface and $A$-phase vortices are not sufficient conditions to trigger the vortex nucleation in the $B$ phase. Besides, a critical counterflow velocity in the $B$ phase must be exceeded. When the cryostat was accelerated at $T \approx T_{AB}$ and $p = 29.3$ bars, $B$-phase vortices were created when the counterflow velocity at the cell wall exceeded the value defined by $\Omega_c \approx 3.2$ rad/s.[4] In the presence of the $AB$ interface, the energy barrier for vortex nucleation was reduced, and $\Omega_c$ decreased from 3.2 to 0.3 rad/s.

It is not yet clear why the $AB$ interface helps the nucleation of MV's and SMV's. One possible process takes place at the line where the $AB$ interface meets the cell

wall.[35] (In the beginning of the $A \rightarrow B$ transition, the line is a circumference at the cell bottom, see Fig. 5.) It involves a continuous transformation of $A$-phase vortices ending at a solid surface to vortices penetrating through the $AB$ interface. In such a process, an existing singularity transforms into another one because the end point of $A$-phase vortex is always singular.[41] Thus the critical velocity should be less than that for vortex nucleation in the cell filled by pure $B$ phase, where singularities have to be created from a nonsingular texture. Nucleation of a SMV instead of a MV is not prevented by topological considerations because a SV can terminate on the $AB$ interface.[41]

To sustain the reversible $A \rightarrow B$ transition, we started by warming the $^3$He sample in the NMR cell from the $B$ to the $A$ phase. The temperature was controlled by means of the nuclear demagnetization stage or by overheating the Pt-NMR coil with rf pulses. As soon as the NMR signal showed a transition to $^3$He-$A$, the temperature drift was reversed and rotation of the cryostat started. To create an equilibrium $A$-phase vortex state, the system was first accelerated to $\Omega = 2.5$ rad/s, after which $\Omega$ was reduced to $\Omega_{AB} = 0.4 - 1.7$ rad/s, the rotation velocity at which the $A \rightarrow B$ transition was to take place. With careful control of temperature, part of the lower section of the cell was kept all the time in the $B$ phase, so that during cooldown the phase front propagated along the 5.5-mm-long tube and through the orifice to the NMR cell (see Fig. 5). The speed at which the front moved across the experimental volume could be estimated from the NMR signal. The slowest average velocities were 0.04 mm/s, while typically the transition occurred in less than a few seconds. The speed of the phase front did not influence strongly the nucleation of SMV's as long as hypercooling was avoided, although it had an effect on the number of MV's in the anomalous state.

In exceptional cases SMV's were observed to form at constant temperature during a rapid acceleration ($\sim 0.1$ rad/s$^2$) of the cryostat to $\Omega = 3$ rad/s $\approx \Omega_c$. Under these conditions, the counterflow velocity at the cell wall could have reached unusually large values, which may have favored the nucleation of SMV's. When the cell was filled with pure $^3$He, this isothermal process was effective at a temperature close to $0.6T_c$. We have also done experiments with $^3$He containing some amount of $^4$He. When the walls of the cell were covered with a superfluid $^3$He-$^4$He film of saturated thickness at $p < 25$ bars ($^4$He solidifies at $p = 25$ bars), the nucleation of SMV's was never observed to occur isothermally. In contrast, if the $^3$He sample with $^4$He was pressurized to 29.3 bars, the state with SMV's formed isothermally more frequently and even at higher temperatures. We believe that in this case the walls of the cell were covered with $^4$He crystallites which provoked the nucleation of SMV's. The $^4$He crystallites had an effect on the nucleation of MV's as well: about 30% smaller $\Omega_c$ values were measured compared with those obtained for pure $^3$He.

Hereafter we concentrate on the reversible $A \rightarrow B$ transition, which provided the most reproducible procedure for creating the SMV's: about 70 reversible transitions with $\Omega_{AB} > 0.4$ rad/s were investigated, and in all cases the anomalous HPD absorption was observed. A superfluid $^3$He-$^4$He film, covering the cell wall, turned out to have little effect on the nucleation of SMV's during the $A \rightarrow B$ transition.

## VII. CONVENTIONAL NMR MEASUREMENTS

The conventional NMR measurement gave two useful pieces of information about the anomalous state created during the $A \rightarrow B$ transition. (i) When the state was studied in the vicinity of $T_{AB}$, immediately after the $A \rightarrow B$ transition, we obtained a spectrum in which the absorption had shifted toward higher frequencies. This initial state decayed with time and, finally, a spectrum was measured which was nearly identical to that from a state with a cluster of MV's. (ii) The spectrum, measured after the decay, was used to determine the number of $B$ phase vortices nucleating during the $A \rightarrow B$ transition. This information was needed for analyzing the $\Omega$ dependence of the anomalous HPD absorption, which led to the identification of the SMV's.

The size of the vortex cluster, formed after the traversal of the $AB$ interface through the NMR cell, was measured as follows: After the $A \rightarrow B$ transition at the rotation velocity $\Omega_{AB}$, the sample was cooled during rotation to about $0.6T_c$ (at this temperature we could produce large numbers of MV's by acceleration[4]), and the NMR spectrum was recorded. Next, a reference state, with known number of MV's, was produced. For this the rotation was stopped in order to remove all MV's and SMV's. After 10 min, the cryostat was accelerated to $\Omega = 3$ rad/s, whereby a large number of MV's, corresponding to $\Omega > 2$ rad/s, were created. $\Omega$ was next reduced to $\Omega_V < 1$ rad/s, and an equilibrium state was formed after the excess vortices had annihilated at the cell walls. A subsequent slow acceleration to $\Omega_{AB}$, during which there was no vortex nucleation, produced a cluster with its number of vortices corresponding to $\Omega_V$. The NMR spectrum was then recorded again, compared with the one measured in the anomalous state and, if the counterflow induced features of the spectra were different, another reference state with a different $\Omega_V$ was prepared. Usually, a few reference states were needed to calibrate the cluster size in the anomalous state with sufficient accuracy. An alternative method to do the calibration is explained below.

An example of the decay of the initial state is shown in Fig. 6. Spectrum 1, recorded 7 min after the $A \rightarrow B$ transition, contains an anomalous peak at the maximum frequency shift $\sin^2\psi = 1$. The peak decays with time through spectra 2 and 3, and finally spectrum 4, recorded 23 min after the transition, shows the signature of the usual flare-out texture, except for the barely visible rounding of the signal edge at $\sin^2\psi \approx 0.8$.

Spectra 1–4 in Fig. 6 were recorded at constant $\Omega = \Omega_{AB} = 1.0$ rad/s. The number of MV's in this anomalous state was so large that the counterflow does not appreciably influence the texture. In order to reach the conditions at which the measurement of $\Omega_V$ could be done

with sufficient resolution, we had to increase $\Omega$ to 1.2 rad/s. During this acceleration, $\Omega_V$ stayed constant and the counterflow peak appeared in spectrum 5, recorded after the acceleration. Because of the large $\Omega_c$ at this temperature, we were not able to create a reference state with a known number of vortices using the recipe described earlier. Instead, the following procedure was employed: $\Omega$ was first decelerated to some value $\Omega_{\rm min}$, then accelerated back to 1.2 rad/s, whereafter the NMR spectrum was remeasured. If the counterflow peak had not increased, we concluded that $\Omega_{\rm min} > \Omega_V$. By successively reducing $\Omega_{\rm min}$ to lower and lower values in these 1.2 rad/s $\rightarrow \Omega_{\rm min} \rightarrow$ 1.2 rad/s deceleration-acceleration cycles, until the counterflow absorption peak started to increase, we could determine the size of the initial unknown cluster.

In the case of Fig. 6, deceleration to $\Omega_{\rm min} = 0.8$ rad/s did not change the intensity of the counterflow peak, but after $\Omega_{\rm min} = 0.75$ rad/s, spectrum 6 was recorded. The counterflow peak had grown more prominent, which indicates that the initial $\Omega_V$ was between 0.75 rad/s and 0.80 rad/s: During the reduction of $\Omega$ to $\Omega_{\rm min} = 0.75$ rad/s the cluster expanded to the wall where a fraction of the vortices were annihilated.

Spectrum 7, which was measured at $\Omega = 1$ rad/s after spectrum 6, has lost all vestiges of metastability; the signal edge at $\sin^2\psi \approx 0.8$ is sharper compared to that in spectrum 4. Although spectra 4 and 7 are almost identical, measurements in the homogeneously precessing resonance mode revealed a quite different picture: A large additional component in the resonance absorption, $P_S$, was still present in state 4, but not in state 7. Compared with the absorption $P_V$ from MV's in a cluster of the same size, this anomalous absorption was typically 10–100 times larger.

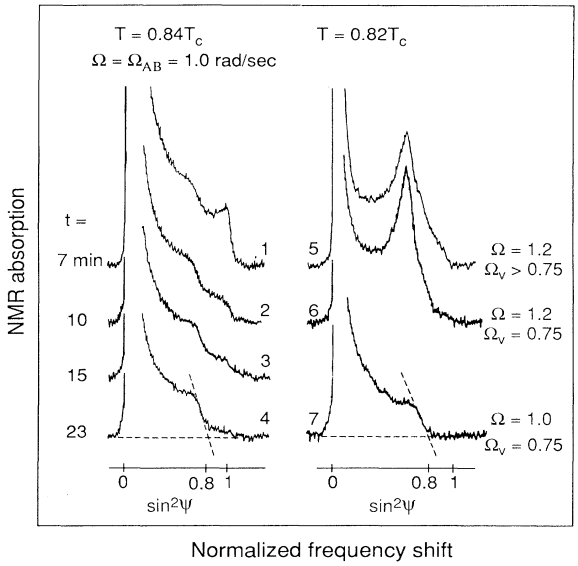


FIG. 6. Signatures of $\theta$ solitons in spectra observed with conventional NMR at low rf excitation. Spectrum 1 was obtained at $t = 7$ min after the $A \rightarrow B$ transition and it contains a peak at the normalized frequency shift $\sin^2\psi = 1$; the peak decays with time. Spectrum 4, measured 23 min after the transition, displays already the standard signature of the flare-out texture. However, the HPD absorption, measured after spectrum 4, shows a well-resolved additional absorption component from $\theta$ solitons, similar to trace 4 in Fig. 7. Spectra 5 and 6 on the right are for calibrating the size of the vortex cluster (see explanation in the text) and were both recorded at $\Omega = 1.2$ rad/s. The number of vortices in spectrum 5 is the same as in spectra 1–4 and corresponds to $0.75 < \Omega_V < 0.8$ rad/s. Spectrum 6 was obtained after reducing $\Omega$ for a moment to 0.75 rad/s. When $\Omega$ was then increased to 1.0 rad/s, spectrum 7 was recorded; it had the clean flare-out shape with a sharp signal edge at $\sin^2\psi \approx 0.8$. In these experiments, $p = 29.3$ bars, $H = 28.4$ mT, and $\mathbf{H} \parallel \mathbf{\Omega}$.

## VIII. HPD ABSORPTION MEASUREMENTS

### A. General characterization of soliton absorption

The course of an experiment utilizing the homogeneously precessing resonance mode is explained in Fig. 7, where we plot the components of the voltage $v_M = v'_M - iv''_M$ induced by the precessing magnetization in the pick-up coil. The curves, which start from the origin and end in a kink at right, were measured at rotation velocities indicated on the plot and correspond to different downward sweeps of the polarizing field $H$. During each sweep, the HPD boundary moved in about 60 s from the top (origin) to the bottom (kink) of the cell.

The components $v'_M$ and $v''_M$ are the dispersion and absorption parts of the NMR signal. The magnitude of $v_M$ is proportional to the projection $|\mathbf{M}_\perp|$ of the total

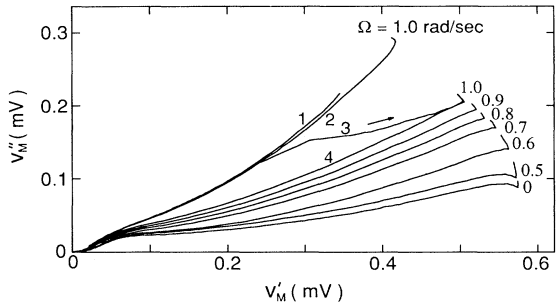


FIG. 7. Signatures of $\theta$ solitons during a measurement of absorption in the HPD. The output from the lock-in amplifier, the absorption ($v''_M$) and dispersion ($v'_M$) signals, is plotted while the HPD boundary was swept through the cell under different but constant values of $\Omega$. At first, a large additional absorption signal in the anomalous state (trace 1) decays spontaneously (via traces 2 and 3), and a more stable structure (trace 4), containing less than half of the initial soliton absorption, is reached. When $\Omega$ is then reduced from 1.0 rad/s to zero, the rest of the additional absorption disappears in a nonlinear fashion. A change $\Delta v''_M = 0.1$ V corresponds to a change $\Delta P = 240$ pW in the absorbed power; on this scale, the absorption caused by mass vortices is not visible. These experiments were done at $p = 29.3$ bars, $T = 0.81\,T_c$, $H = 14.2$ mT, $\nabla H = 5$ mT/m, $\Omega_{AB} = 1.0$ rad/s, and $\mathbf{H} \parallel \mathbf{\Omega}$.

precessing magnetization on the plane ($\perp \mathbf{H}$) which contains the axis of the rf pick-up coil. Because of the homogeneity of the HPD, $|v_M|$ is under most experimental circumstances proportional to the volume of the precessing domain. The phase of $v_M$, i.e., the angle $\alpha$ between $\mathbf{M}_\perp$ and $\mathbf{H}_{\rm rf}$, is determined by the energy dissipation $P$ in the HPD and by a correction term proportional to $|v_M|^2$ [7,42] (in the simplest case, if the correction term is neglected, $P = \gamma|\mathbf{M}_\perp|\omega H_{\rm rf}\sin\alpha$). Especially, if $|v_M|$ stays constant, $\Delta v_M''$ is directly proportional to $\Delta P$. The maximum power supply from the rf field corresponds to $\sin\alpha = 1$; if $\alpha$ reaches the value 90° the HPD collapses.

A thorough discussion of the relaxation mechanisms defining the absorption $P_{\Omega=0}$ along the lowermost curve in Fig. 7, measured in the stationary state, is presented in Ref. 7. The spin-diffusion relaxation within the HPD boundary, $P_B$, is responsible for the rapid increase in the absorption near the origin, when the HPD boundary appears at the top of the cell. When the HPD boundary is swept to the bottom of the cell, this absorption component disappears, which produces the minimum in the kink at right. When the HPD fills the whole cell, the Leggett-Takagi relaxation[33] is the dominant mechanism. Counterflow[9,8] and vortices[10,8] modify slightly $P$, but their effect is negligible compared to the anomalous absorption in Fig. 7, to be discussed next.

Similarly with conventional NMR experiments, the HPD absorption measurements revealed an unstable high-absorption state, present immediately after the $A \rightarrow B$ transition. It rapidly decayed to a more stable state displaying smaller additional absorption. The order in which the four curves at $\Omega = \Omega_{AB} = 1$ rad/s in Fig. 7 were recorded is indicated by the numbering of the consecutive field sweeps. During the first sweep (curve 1), which was made right after the $A \rightarrow B$ transition, the absorption in some part of the cell grew larger than the maximum power supply from the rf field, and the HPD collapsed. During the second half of the third sweep, the state decayed in about 30 s to a more stable configuration, containing less than half of the absorption $P_S = P_{\rm tot} - P_{\Omega=0}$ of the initial state. This state (curve 4) is more stable: cooling to $0.55\,T_c$ or a change in the rotation velocity from $\Omega_{AB} = 1.0$ rad/s to 2.8 rad/s and back to $\Omega_{AB}$ did not reduce $P_S$. The anomalous absorption increases roughly linearly with the HPD volume which shows that it has a constant distribution along the $\boldsymbol{\Omega}$ axis. $P_S$ depends on $\Omega$ in a nonlinear way. Variations in $P_S$ from one cooldown to the next could be almost an order of magnitude but, nevertheless, some features common to all these states were observed.

The most valuable information for identifying the source of the anomalous absorption was the dependence of $P_S$ on the rotation velocity. The additional absorption, measured when the HPD fills the whole NMR cell (which corresponds to the kinks in Fig. 7), is plotted in Fig. 8 as a function of $\Omega$ after three different cooldowns from the $A$ phase. All these curves contain a portion showing the dependence $P_S(\Omega) \propto 1 - \sqrt{\Omega^*/\Omega}$, which extrapolates to zero when $\Omega$ is reduced to some critical $\Omega^*$. This value coincides with $\Omega_V$, which is determined from the conventional NMR spectra. As long as $\Omega$ was kept

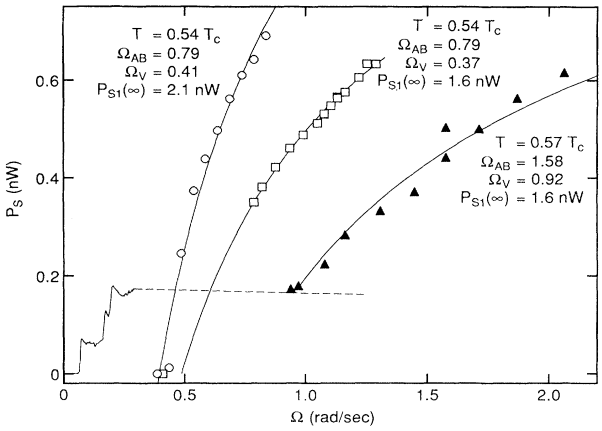


FIG. 8. Anomalous HPD absorption $P_S$ as a function of the rotation velocity after three cooldowns from the $A$ phase at constant $\Omega = \Omega_{AB}$. The curved lines show the fit of the dependence $P_S = P_{S1}(\infty)(1 - \sqrt{\Omega^*/\Omega})$ to the measured data, with fitting parameters $P_{S1}(\infty)$ and $\Omega^*$. The critical rotation velocity $\Omega^*$, at which the $\Omega$-dependent part of $P_S$ disappears, agrees with $\Omega_V$, which was obtained by using conventional NMR. $\Omega_V$ is the angular velocity at which the vortex cluster expands to the cell wall. The dataset with $\Omega_{AB} = 1.58$ rad/s shows a nearly $\Omega$-independent component (dashed line and recorder trace) which decays in a stepwise manner at $\Omega < 0.2$ rad/s. In these experiments, $p = 29.3$ bars, $H = 28.4$ mT, $\nabla H = 0.15$ mT/m, and $\mathbf{H} \parallel \boldsymbol{\Omega}$.

sufficiently above $\Omega^*$, it could be changed up and down without affecting $P_S(\Omega)$; if $\Omega$ was reduced to $\Omega^*$, this type of anomalous absorption did not reappear even if $\Omega$ was again increased to a value higher than $\Omega^*$.

The curve with $\Omega_{AB} = 1.58$ rad/s in Fig. 8 shows, besides the square-root dependent component, a nearly $\Omega$-independent part at low velocities $\Omega < \Omega^*$. This constant absorption could persist, when $\Omega$ was being reduced, to rotation velocities less than 0.1 rad/s, and sometimes it decayed in steps of equal magnitude. The set of data in Fig. 8, containing the $\Omega$ independent part, has three such steps at $\Omega < 0.2$ rad/s. The two components in the anomalous absorption originate from different parts in the cell. The $\Omega$-dependent component disappears when the vortex cluster touches the cell wall at $\Omega = \Omega_V$ and is, therefore, clearly supported by the counterflow outside the cluster, while the $\Omega$-independent part, which also exists in the absence of the counterflow layer, originates from the vortex cluster.

### B. $\Omega$ dependence of HPD absorption from $\theta$ solitons

We argue that the anomalous absorption in Fig. 8 is caused by $\theta$ solitons attached to SMV's. These solitons stretch from the top to the bottom of the NMR cell and appear in two configurations, presented in Fig. 1. We associate the absorption $P_{S1}$, that has square-root dependence on $\Omega$, with the solitons that stretch between a single SMV and the side wall of the cell. The nearly $\Omega$-independent absorption $P_{S2}$ we associate with the SMV pairs bound by solitons.

The $\theta$ solitons enhance the absorption in the HPD through the spin-diffusion relaxation. This will be discussed in Sec. VIII C. Here we begin by assuming that $P_S$ is proportional to the area of the soliton, if the length $\tilde{L}$ of the HPD is kept fixed, and show that the model of two different configurations of $\theta$ solitons can explain all the observed features in the $\Omega$ dependence of $P_S$.

The position of the SMV in the counterflow region and the distance between the two SMV's in the pair are determined by the balance of the Magnus force acting on the MV part of SMV and the soliton tension. Because the dipolar energy is not minimized in the soliton, it has surface tension $\sigma \approx 2.0 g_D \xi_D$,[12] which tends to reduce the width of the soliton. In the case of a soliton in the counterflow layer, $\sigma$ can be compensated by the Magnus force $F_M = \rho_s \kappa (v_s - v_L) = \rho_s \kappa (\Omega_V R^2/r - \Omega r)$, directed toward the center of the cell. Here $v_L$ is the velocity of the SMV which, like all the other defects, have to move with the normal component in equilibrium. Therefore, $v_L = v_n = \Omega r$. The equilibrium position of the SMV, $r = R - \ell$, is determined by the condition $F_M = \sigma$, which gives the $\Omega$ dependence of the width $\ell$ of the soliton, viz.,

$$\frac{\ell(\Omega)}{R} = 1 - \frac{\Omega_S}{2\Omega} - \sqrt{\frac{\Omega_V}{\Omega} + \left(\frac{\Omega_S}{2\Omega}\right)^2} \quad . \tag{13}$$

Here $\Omega_S = \sigma/(\rho_s \kappa R)$. When $\Omega$ decreases to the critical value $\Omega^* = \Omega_S + \Omega_V$, the width of the soliton approaches zero and it annihilates on the wall. Using the values $g_D \approx 7.5 \times 10^{-6}$ J/m$^3$ and $\xi_D = 16$ $\mu$m appropriate at $T = 0.7 T_c$ and $p = 29.3$ bars, one obtains $\Omega_S \approx 0.05$ rad/s $\ll \Omega_V$, in agreement with the experimental observation $\Omega^* \approx \Omega_V$. This means that the SMV is located outside but close to the edge of the cluster and that $P_{S1}$, assuming that it is proportional to the width $\ell$ of the soliton, has the form

$$P_{S1}(\Omega) = P_{S1}(\infty)\frac{\ell(\Omega)}{R} \approx P_{S1}(\infty)\left(1 - \sqrt{\frac{\Omega_V}{\Omega}}\right) \quad , \tag{14}$$

where the saturation value $P_{S1}(\infty)$ corresponds to $\ell = R$. This analysis explains the $\Omega$ dependent part of $P_S$ in Fig. 8.

A pair of SMV's, bound by the soliton, resembles a doubly quantized mass vortex: the total winding numbers are $\nu = 1 + 1 = 2$ and $\nu_R = 1 + 1 = 0$. The distance $d$ of the SMV's in the pair is determined by the balance between the repulsion of the MV parts and the attraction of the SV parts. The repulsive Magnus force $F_M = \kappa^2 \rho_s/(2\pi d)$ arises between mass vortices with the same sign of circulation. The interaction between the SV parts is proportional to $1/d$ when $d \ll \xi_D$, which corresponds to a kind of Magnus force for spin current and is attractive since a SV is equivalent to its antivortex. At larger distances $d \gg \xi_D$, when the soliton tail is well developed, the attraction is given by the soliton tension. If one approximates the attractive forces by the soliton tension $\sigma$ only, one obtains an upper limit $d \leq \rho_s \kappa^2/(2\pi\sigma)$ which is about $6\,\xi_D$ close to $T_c$. This is less than the average spacing between MV's in the vortex lattice ($\approx 200$ $\mu$m at $\Omega = 1$ rad/s). Therefore, $d$ is expected to decrease only slightly with increasing $\Omega$ when the SMV pair is placed among the other vortices in the rotating liquid. Consequently, the HPD absorption from the SMV pair is nearly independent of $\Omega$. This explains the weakly $\Omega$ dependent part $P_{S2}$. Its stepwise decay arises from annihilations of solitons.

In addition to the $\Omega$ dependence of the $P_{S1}$ and $P_{S2}$, the following arguments support the identification of solitons as the source of the additional absorption.

(i) There is experimental evidence that both $P_{S1}$ and $P_{S2}$ are caused by several identical objects, i.e., the absorption in the anomalous state is a discrete quantity which corresponds to several independent solitons, see Sec. IX.

(ii) The magnitude of the anomalous absorption agrees roughly with a simple theoretical estimate, see Sec. IX C.

(iii) The boundary of the HPD can be moved by sweeping the magnitude of $H$. Thus one may trace out the distribution of $P_S$ in the NMR cell. $P_{S1}$ and $P_{S2}$ show distinct power laws as a function of the HPD length and field gradient. These agree with the theoretical ones, see Sec. VIII C.

(iv) The combination of a SMV and a soliton is a unique structure that can explain both the observed stability and the low characteristic velocities appearing in Fig. 8. On the one hand, the high stability of the object is a consequence of two factors: both the MV and the SV-soliton pair are topologically stable, and the binding between the SV and the MV is caused by the high-energy structure of the vortex core. This structure cannot be destroyed by hydrodynamic (changes in $\Omega$) or magnetic (switching on and off HPD) perturbations. On the other hand, the positional stability of the SMV is determined by the much weaker forces that originate from the dipole-dipole interaction and the long-range mass flow around the MV's. Other possible objects we know of are either pure soft structures or pure hard structures. Examples of the former are $\hat{\mathbf{n}}$ or $\theta$ solitons without a SMV or metastable $\hat{\mathbf{n}}$ textures. These cannot explain the stability of the anomalous absorption because they are completely swept out by the HPD and can also be "annealed" away by rotation. The scales of velocities in Fig. 8 cannot be explained by pure hard structures because they have a characteristic velocity on the order of the pair-breaking velocity ($\approx 10$ cm/s). For example, a multiply quantized vortex in the vortex cluster should give a constant $P_S(\Omega)$. A hard structure in the counterflow zone (e.g., a surface state) does not explain why $P_S$ depends sensitively on $\mathbf{v}_s - \mathbf{v}_n$ at such small velocities as $|\mathbf{v}_s - \mathbf{v}_n| \sim R\Omega_S$.

In general, all our observations seem to be consistent with the SMV's. The puzzling exception is that the temperature dependence of the anomalous absorption remains unexplained (see last paragraph of Sec. IX C).

### C. Spin-diffusion relaxation from $\theta$ solitons

Figure 4 presented two ways for the $\theta$ soliton to coexist with the HPD. Our experiments support the static

structure for the soliton in the counterflow zone but for the SMV pairs the structure cannot be resolved.

We associate the anomalous absorption $P_S$ with the spin-diffusion relaxation which is induced by the inhomogeneity in the magnetization. The absorption due to spin diffusion is proportional to $D\int dV|\nabla_i \mathbf{M}|^2$. Here $D$ is the spin-diffusion coefficient, and we neglect the tensor character of $D$ as well as deviations from diffusion theory. Let us consider the case that $\mathbf{H}$ is parallel to $\mathbf{\Omega}$ and the soliton wall. The absorption $P_B$ of the free HPD boundary is proportional to $DM^2\pi R^2/\lambda_0$, where $\pi R^2$ is the area and $\lambda_0$ the thickness of the boundary (Sec. IV C). The absorption in the dynamic soliton [Fig. 4(a)] is proportional to $DM^2\ell\tilde{L}/\xi_D$, where $\ell\tilde{L}$ is the area of the soliton within the HPD ($\ell$ is the width of the soliton and $\tilde{L}$ is the HPD length) and $\xi_D$ characterizes the thickness of the soliton. The thickness of the region of inhomogeneous magnetization in the static soliton [Fig. 4(b)] depends on $z$ and is on the order of

$$\xi_\omega(z) = [c^2/(z-z_0)\omega\gamma\nabla H]^{1/2} = \lambda_0\sqrt{\lambda_0/(z-z_0)}.$$

Therefore the absorption is

$$P_S(\text{static}) \propto DM^2\ell\int_{z_0}^{L}\frac{dz}{\xi_\omega(z)} = \frac{2}{3}DM^2\ell\left(\frac{\tilde{L}}{\lambda_0}\right)^{3/2}. \quad (15)$$

Thus the expected dependences on $\tilde{L}$ and $\nabla H$ for the two types of solitons are $P_S(\text{static}) \propto \tilde{L}^{3/2}(\nabla H)^{1/2}$ and $P_S(\text{dynamic}) \propto \tilde{L}(\nabla H)^0$.

This analysis is valid if the soliton can be considered as a sheet, i.e., its width and height are much larger than the thickness: $\ell, \tilde{L} \gg \xi_\omega$ or $\xi_D$. In a SMV pair the width of the soliton is comparable to its thickness, and the soliton should be considered as a linear object, for which the spin-diffusion absorption does not depend on the thickness of the soliton: $D\int dV|\nabla_i\mathbf{M}|^2 \sim DM^2\tilde{L}$. In this case, $P_S \propto \tilde{L}(\nabla H)^0$, regardless of the type of the soliton. For this reason, the difference between static and dynamic solitons can be experimentally resolved only for the solitons in the counterflow zone.

Figure 9 shows the results from an experiment on one sample of SMV's in which $P_S$ was measured as a function of $\tilde{L}/L$ while $\Omega$ was successively reduced to lower values. This analysis allows the division of $P_S$ to $P_{S1}(\tilde{L}/L)$ for the solitons in the counterflow zone and $P_{S2}(\tilde{L}/L)$ for the solitons in the vortex cluster. The inset displays the $\Omega$ dependence of $P_S$ measured when the HPD filled the whole NMR cell. The solitons in the counterflow layer are clearly present when $\Omega \geq 0.8$ rad/s. The curve in the inset shows the fit to the formula $P_S(\Omega) = P_S(\infty)(1-\sqrt{\Omega^*/\Omega})$. Here we have used different abbreviations for the fitting parameters than in Eq. (14), because $P_S(\Omega)$ contains some (so far) unknown constant contribution $P_{S2}$ from solitons in the

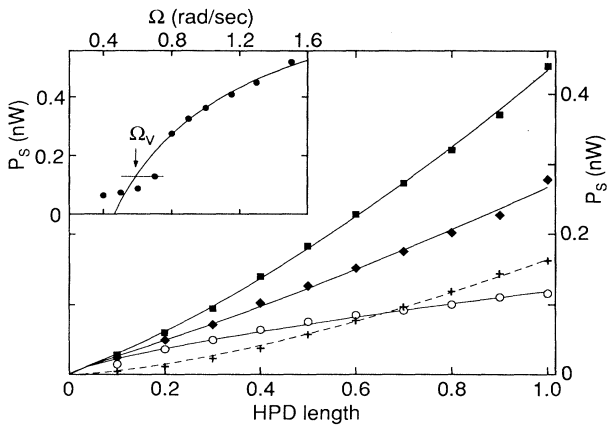


FIG. 9. The distribution of $P_S$ analyzed as a function of both the relative HPD length $\tilde{L}/L$ and the rotation velocity $\Omega$ for one sample of SMV's: squares, $\Omega = 1.3$ rad/s; diamonds, 0.8 rad/s; circles, 0.7 rad/s. Both solitons in the vortex cluster and in the counterflow zone contribute to squares and diamonds, whereas the circles show only $P_{S2}$ from solitons in the vortex cluster. The crosses show $P_S(\tilde{L}/L, 1.3$ rad/s$) - P_S(\tilde{L}/L, 0.8$ rad/s); the meaning of the curves is explained in the text. In the inset $P_S$ is plotted as a function of the rotation velocity $\Omega$ when the HPD fills the whole cell. This measurement was done at $p = 29.3$ bars, in $T = 0.76\,T_c$, $H = 14.2$ mT, $\nabla H = 4.6$ mT/m, and $\mathbf{H} \parallel \mathbf{\Omega}$.

vortex cluster (i.e., $P_S(\Omega) = P_{S2} + P_{S1}(\infty)(1-\sqrt{\Omega_V/\Omega})$, which gives relations $P_S(\infty) = P_{S2} + P_{S1}(\infty)$ and $\Omega^* = \{P_{S1}(\infty)/[P_{S2} + P_{S1}(\infty)]\}^2\Omega_V$). Data in the inset measured at $\Omega = 0.7$ and 0.6 rad/s fall considerably below the fit; there only solitons in the counterflow layer remain.

The analysis of $P_S$ as a function of the length of the HPD is shown in the main part of Fig. 9. We extracted $P_S(\tilde{L}/L) = P_{\text{tot}}(\tilde{L}/L) - P_{\Omega=0}(\tilde{L}/L)$ from plots such as in Fig. 7. The relative length of the HPD, $\tilde{L}/L$, is obtained by dividing $|v_M|$, the total voltage induced in the pick-up coil from the HPD, by the maximum value of $|v_M|$, measured when the HPD fills the entire cell. The circles, diamonds, and squares in Fig. 9 depict $P_S(\tilde{L}/L)$ at different rotation velocities. Because the number of solitons is not changing between $\Omega = 1.3$ and 0.8 rad/s, the $\tilde{L}/L$ dependence of $P_{S1}$ is obtained most reliably by subtracting $P_S(\tilde{L}/L, 0.8$ rad/s$)$ from $P_S(\tilde{L}/L, 1.3$ rad/s$)$. The result is shown by the crosses; the broken curve illustrates the dependence $P_{S1}(\tilde{L}) \propto (\tilde{L}/L)^{3/2}$ of the static solitons, which fits adequately to our data. At $\Omega \leq 0.7$ rad/s the data in Fig. 9 share a $\tilde{L}/L$ dependence which is clearly different from the $(\tilde{L}/L)^{3/2}$ proportionality assigned to solitons in the counterflow layer. It thus appears that all the solitons in the counterflow layer have annihilated at $\Omega \geq 0.7$ rad/s and at $\Omega = 0.7$ rad/s $P_S(\tilde{L}/L) = P_{S2}(\tilde{L}/L)$. A fit to the formula $P_{S2}(\tilde{L}/L) = p_2(\tilde{L}/L)^{\nu_2}$ gives the exponent $\nu_2 = 0.73$ (see the curve through the circles in the main part of Fig. 9). Similar analyses for velocities $\Omega < 0.7$ rad/s in this run and for other runs produced values ranging from 0.7 to 0.9. This is close to the linear dependence predicted for

a line object. The small deviation of $\nu_2$ from 1 may be readily explained in terms of corrections of order $\xi_\omega/\tilde{L}$ for the static soliton or by the corrections of order $\xi_D/\xi_\omega$ for the dynamic soliton.

In order to find the $\Omega_V$ and check the consistency of the analysis in Fig. 9 we have fitted the formula $P_S(\tilde{L}/L) = p_1(\tilde{L}/L)^{3/2} + p_2(\tilde{L}/L)^{0.73}$ to the data measured at $\Omega = 1.3$ and 0.8 rad/s. These fits, shown by the lines in the figure, give $p_2 = 104$ pW ($\Omega = 1.3$ rad/s) and $p_2 = 114$ pW ($\Omega = 0.8$ rad/s), which are close to the measured $P_S(0.7\,\text{rad/s}) = 119$ pW. These three values, 104, 114, and 119 pW correspond to the absorption from the solitons inside the vortex cluster and since they agree with each other (within our experimental uncertainties) it means that the number of SMV pairs in the cluster does not change during deceleration from 1.3 to 0.7 rad/s. Thus $\Omega_V$, which gives the initial number of vortices, can be found from the intersection of the fit to the formula $P_S(\Omega) = P_{S1}(\infty)(1 - \sqrt{\Omega^*/\Omega})$, shown by the solid line in the inset, and the horizontal line that goes through the point $P_S(0.7\,\text{rad/s})$. It is found to be $\Omega_V \approx 0.6$ rad/s. Unfortunately, in this experiment $\Omega_V$ was not measured independently using the conventional NMR method. The tendency that the solitons in the counterflow zone annihilate at rotation velocities larger than $\Omega_V$ was observed quite often.

In a few experiments, a similar analysis as that in Fig. 9 gave a result that the nearly $\Omega$-independent absorption component $P_{S2}$ must have been considerably larger at $\Omega > \Omega_V$ than what was measured after deceleration to $\Omega < \Omega_V$. This can be explained by assuming that in these runs the bound pairs of SMV's were concentrated to the edge of the vortex cluster and a large part of them annihilated at $\Omega \approx \Omega_V$.

Further characteristics of the solitons in the counterflow layer were obtained from experiments in which the magnetic field gradient was varied. The lower part of Fig. 10 contains $P_S(\tilde{L}/L)$ curves which were measured at $\Omega = 1$ rad/s with five different $\nabla H$ for one anomalous state which is different from the one analyzed in Fig. 9. In this example the number of SMV pairs in the cluster is small; a fit to the dependence $P_{S1}(\tilde{L}/L) = p_1(\tilde{L}/L)^{3/2}$ explains well the data at different $\nabla H$ and also at different $\Omega$ (not shown in the figure). The parameter $p_1$, given by the fits in the region $0.2 \le \tilde{L}/L \le 0.9$ to the data in the lower part of Fig. 10, is presented as a function of $\nabla H$ in the inset on the right; the curve shows the $\sqrt{\nabla H}$ dependence which should be obeyed by the static solitons. This agrees well with the measurement, although one should take a cautious attitude toward the data measured at the lowest $\nabla H$, where the width of the HPD boundary starts to be sizable compared with the dimensions of the cell, $\lambda_o/L \approx 0.08$. The inset on the left in Fig. 10 shows $P_S(\Omega)$ when $\tilde{L}/L = 1$ and $\nabla H = 4.6$ mT/m. We conclude that here $\Omega_V \approx 0.5$ rad/s and the solitons in the counterflow zone annihilate between $\Omega = 0.6-0.7$ rad/s. The remaining $P_{S2}$ component at $\Omega = 0.6$ rad/s could not be extracted from the $P_S(\tilde{L}/L)$ curves at $\Omega > 0.6$ rad/s: it is either lost to the scatter of the data or, more intriguing possibility, in this example the solitons in the vortex cluster are produced from the solitons in the counterflow zone (which process is shortly discussed in Sec. IX A).

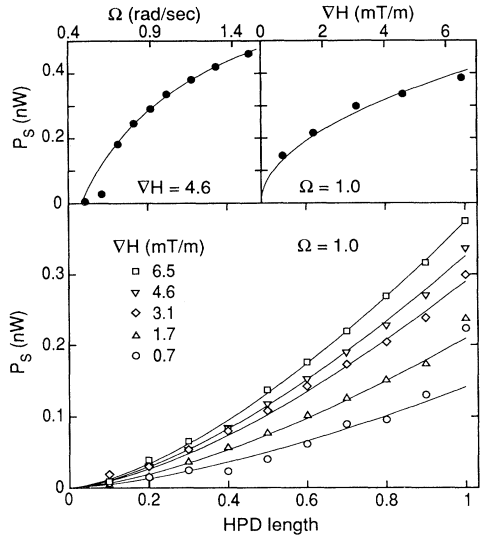


FIG. 10. Dependence of the additional absorption from $\theta$ solitons on the magnetic field gradient. In the lower part of the figure, $P_S$, measured at constant $\Omega = 1$ rad/s, is plotted as a function of the relative HPD length $\tilde{L}/L$ at five field gradients for the same sample of SMV's. Lines show fits of the form $P_S(\tilde{L}/L) = p_1(\tilde{L}/L)^{3/2}$. The parameter $p_1$, given by the fits, is presented as a function of $\nabla H$ in the inset on the right. The inset on the left displays $P_S(\Omega)$ at $\nabla H = 4.6$ mT/m and for $\tilde{L}/L = 1$, measured for the same anomalous state as in the lower part. In these experiments, $p = 29.3$ bars, $T = 0.76\,T_c$, $H = 14.2$ mT, and $\mathbf{H} \parallel \mathbf{\Omega}$.

When the HPD boundary is swept near the cell bottom ($\tilde{L}/L \approx 1$), $P_{S1}$ increases to a value higher than that given by an extrapolation from the region $\tilde{L}/L < 0.9$ (see Fig. 10). This effect is largest at small $\nabla H$ and may indicate that the HPD-NPD interface, coating the soliton, is modified near the cell bottom.

The absorption from solitons in the vortex cluster depends on the field gradient only weakly. In contrast to solitons outside the cluster, a small decrease in $P_{S2}$ was measured with increasing $\nabla H$: at $H = 14.2$ mT and $T = 0.78\,T_c$ a change in $\nabla H$ from 3.5 to 8.5 mT/m resulted in a 15% decrease in $P_S$. If we assume that $P_{S2} \propto \int dz(\omega - \gamma H)^{\nu_2 - 1}$, we obtain the $(\tilde{L}/L)^{\nu_2}$ and $\nabla H^{\nu_2 - 1}$ dependences. The measured $\tilde{L}$ and $\nabla H$ dependences both give $\nu_2 < 1$ but close to unity, which is consistent with the assumption that solitons in the vortex cluster are nearly line objects.

The data analysis presented in this section assumes that the HPD volume $\pi R^2 \tilde{L}$ is directly proportional to the amplitude $|v_M|$. This is well grounded if the rf field is intense enough to keep the phase of the spin precession uniform, which is not always the case in the present experiments: $P_S$ is localized to narrow regions in the cell, which can cause gradients in the spin precession. Such an effect is clearly detectable in Fig. 7: the voltage $|v_M| = \sqrt{(v_M')^2 + (v_M'')^2}$, measured at the kink for the

state marked by the number 4, is 6% smaller than the corresponding signal in the stationary state with no solitons. During the measurement of Figs. 9 and 10, the homogeneity of spin precession was rather good: the maximum value of $|v_M|$ was only 3% smaller at $\Omega = 1.3$ rad/s than at $\Omega = 0$. Such a small reduction in $|v_M|$ cannot affect the analysis presented in Figs. 9 and 10, especially since $P_S$ increases nearly linearly with $\tilde{L}/L$, which means that the reduction in $|v_M|$ should be rather evenly distributed along the length of the HPD.

### D. Experiments in transverse field H⊥Ω

Experiments during which the length of the HPD was varied in an axial field showed that the solitons extend from the top to the bottom of the cell. Measurements in a transverse field, $\mathbf{H}\perp\mathbf{\Omega}$, by sweeping the HPD boundary (which was parallel to $\mathbf{\Omega}$ axis) across the NMR cell, revealed additional features about the spatial distribution of $P_S$. Variations from one run to the next or even between two consecutive sweeps of the HPD boundary through the same anomalous state were large and depended on the sweep rate. In most cases the central parts of the cell seemed to contribute less to the absorption than the counterflow layer. This is what we expect after our studies of $P_S(\Omega)$ in an axial field, in which the square-root dependent contribution, produced in the counterflow layer, is typically ten times larger than the $\Omega$-independent part, originating from the vortex cluster.

An example of an experiment in a transverse magnetic field is shown in Fig. 11. While $H$ was swept up or down, the domain boundary, parallel to $\mathbf{\Omega}$, moved through the cell, and the NMR absorption was recorded as a function of the HPD volume. From the total absorption in the anomalous state we subtracted the signal in a reference state, for which a vortex cluster with $N = 0.5\,N_{\rm eq}$ was selected. The resulting $P_S$ is plotted in Fig. 11. Three observations deserve comments: (i) There is large hysteresis in $P_S$ between downward and upward sweeps of $H$, i.e., for increasing and decreasing the HPD volume. (ii) Abrupt steps toward decreasing absorption are seen in $P_S$ and (iii) the overall fluctuation of absorption is large. The presence of hysteresis did not depend on the rate at which the domain wall moved, but the steps appeared only at very low values of $dH/dt$; in this example the field sweep in one direction took 10 min.

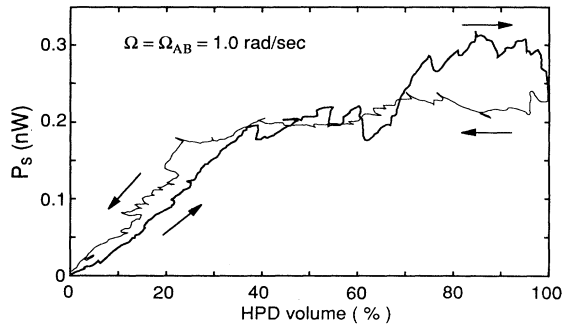


FIG. 11. Anomalous absorption, as a function of the HPD volume in the transverse field orientation. The domain boundary is a plane parallel with $\mathbf{\Omega}$ and moves sideways through the NMR cell. The abrupt steps (with increasing HPD volume) and the nonmonotonous behavior (decreasing volume) display an interaction of the domain wall with a $\theta$ soliton. Comparison with Fig. 7 (in which $P_S$ is of the same magnitude as here) proves that the large fluctuations in the additional resonance absorption are not due to noise in the spectrometer but arise from the motion of solitons. In these experiments, $p = 29.3$ bars, $T = 0.66\,T_c$, $H = 14.2$ mT, and $\mathbf{H} \perp \mathbf{\Omega}$.

We believe that all these features are connected with the motion of solitons. In particular, the observed hysteresis might indicate that solitons interact strongly with the domain wall: they are either pushed in front of the advancing boundary outside the precessing domain or in front of the retreating boundary within the HPD. The SMV's and the end point of the soliton at the wall jump from one pinning site to another, which may account for the steps in $P_S$. The surface energy of solitons increases when they move into the HPD. This can explain why the solitons are pushed in front of the advancing HPD.

Although the behavior in Fig. 11 is complex we conclude that this does not contradict the conclusion that $\theta$ solitons are the explanation for the additional resonance absorption.

## IX. NUMBER OF SOLITONS

Our experiments provide a rough estimate for the additional HPD absorption caused by a single soliton. In the case of a soliton in the counterflow layer, Eq. (14) was fitted to $P_{S1}(\Omega)$ scans corresponding to numerous anomalous states and the value of $P_{S1}(\infty)$, which refers to a single soliton, was deduced from the distribution of the fitting parameters (Sec. IX B). The $P_{S2}$ produced by a soliton in the vortex cluster was obtained more directly: these solitons were seen sometimes to annihilate one by one (Sec. IX C). After the decay of the initial state showing high absorption, we observed, on the average, two solitons in the counterflow layer. The variation of the number of solitons in the vortex cluster was large. Typically there were a few of them, but occasionally $P_{S2}$ corresponded to up to 20 solitons in the cluster. In these cases, the number of SMV's, about 40, was typically one tenth of the total number of vortices.

### A. The initial state

In the initial state, right after the $A \rightarrow B$ transition, the number of $\theta$ solitons may be considerably larger than in a later, more stable situation. This is reflected in the conventional NMR spectra of Fig. 6. Our belief is that, because of their small volume, $\theta$ solitons are not seen directly in the conventional NMR spectra: only the $\hat{\mathbf{n}}$ texture associated with a soliton is observed. $\hat{\mathbf{n}}$ tends to be perpendicular to the soliton wall. In a field $\mathbf{H} \parallel \mathbf{\Omega}$, this produces a peak in the NMR spectra at $\sin^2\psi = 1$. If we simply take the absorption at $\sin^2\psi = 1$ as a measure of

the soliton number, the state represented by spectrum 4 in Fig. 6 would contain only $\approx 10\%$ of the solitons present in the state producing spectrum 1.

However, it is not completely clear, in which way the texture is deformed in the initial state. The appearance of an additional peak at the maximum frequency shift is not the only change: compared with spectrum 4 (or 7), spectra 1, 2, and 3 in Fig. 6 have clearly increased absorption at frequency shifts $\sin^2\psi > 0.2$. Since the integrated NMR absorption in the signal is constant, the extra absorption at $\sin^2\psi > 0.2$ is coming from the peak near the Larmor edge $\sin^2\psi = 0$. This means that in the initial state the solitons distort the texture throughout the cell, not only locally in the counterflow region. After the decay of the initial state, the few solitons in the counterflow layer do not show up clearly in the NMR spectrum, as can be seen from Fig. 6 by comparing spectrum 7, with no solitons in the counterflow layer, with spectrum 4 for which additional $\Omega$-dependent HPD absorption was measured. The absorption at $0.8 < \sin^2\psi < 1$ in spectrum 4 is about 1% of the integrated absorption in the whole signal. This is a reasonable order of magnitude: The volume of the $\hat{\mathbf{n}}$ textures influenced by the soliton, compared with the volume of the cell, is roughly $2\ell\xi_H/\pi R^2 \approx 2\%$, assuming that $\Omega = 2\Omega_V$ and $\xi_H = 0.4\,\mathrm{mm}$, appropriate at $H = 28.4\,\mathrm{mT}$ and $T \approx T_{AB}$. This estimate gives the upper limit because the main forces orienting $\hat{\mathbf{n}}$ outside the vortex cluster and far from the solitons are due to the cell wall and counterflow $\mathbf{v}_s - \mathbf{v}_n$. For example, the counterflow determines a length on the order of $\xi_H v_D/(v_s - v_n)$, which is $0.3\xi_H$ close to the cell wall in a typical case with $\Omega = 2\Omega_V = 1\,\mathrm{rad/s}$ and $v_D \approx 0.5\,\mathrm{mm/s}$.

In the initial state, a large number of $\theta$ solitons may form a tangle, which causes the distortions in the spectra. To explain the decay of the initial state, one can imagine two ways in which the number of solitons can be reduced. (i) If two solitons meet, a rearrangement is possible which does not change the SMV number but minimizes the width of the solitons. For example, if two solitons in the counterflow region touch or intersect each other they annihilate at the site of the contact since they obey the summation rule $1 + 1 = 0$. Two solitons are formed: a soliton between the two SMV's and a soliton which has both ends at the wall. The former binds the two SMV's to a pair while the latter shrinks and finally annihilates at the wall.

(ii) A SMV may dissociate into a MV and a SV. Because this requires a considerable amount of energy, the process likely takes place only in a collision with another singular line. The soliton attached to the SV then shrinks to the wall or to another SMV, since the tension of the soliton is no more compensated by the Magnus force. The dissociation occurs first at one point, from where the reaction proceeds over the whole length of the SMV. Like in nuclear reactions, such a process needs overcoming the energy barrier caused by the repulsion of vortices of the same sign of circulation, which corresponds to the Coulomb repulsion of nuclei. Both scenarios (i) and (ii) may occur during the decay of the initial state, while (ii) is responsible for the stepwise decay of $P_S$, which will be discussed in Sec. IX C.

In the HPD mode, the initial state after the $A \rightarrow B$ transition showed a very large absorption. In many cases we were not able to create the HPD, or if it formed, it collapsed early, already when it filled only a portion of the cell. At the moment of destruction, $P_S$ could be four times larger than the value measured after the decay of the initial state at the same HPD volume. Generally, the HPD collapses if the power absorption exceeds the level of the rf excitation, and thus, by increasing the rf field, the HPD can be made more stable. However, a peculiar feature in the collapse was noticed in the initial state: the change always took place at about the same HPD volume, irrespective of the strength of the rf field. At a certain HPD volume, an instability occurred which could not be overcome by increasing the power supplied from the rf field. A similar feature was observed after the decay of the initial state, when $P_S$ was studied under high field gradients. At $\nabla H \approx 10\,\mathrm{mT/m}$, the HPD usually collapsed during the sweep of the domain boundary across the cell; doubling the rf field intensity did not change noticeably this behavior.

### B. Solitons in the counterflow zone

The temperature dependence of the parameter $P_{S1}(\infty)$ is shown in Fig. 12. Measurements were made when the HPD filled the entire cell, and each experimental point is given by fitting Eq. (14) to the $P_{S1}(\Omega)$ data, which were obtained after different cooldowns from the $A$ phase and after the decay of the initial state. $P_{S1}(\Omega)$ was de-

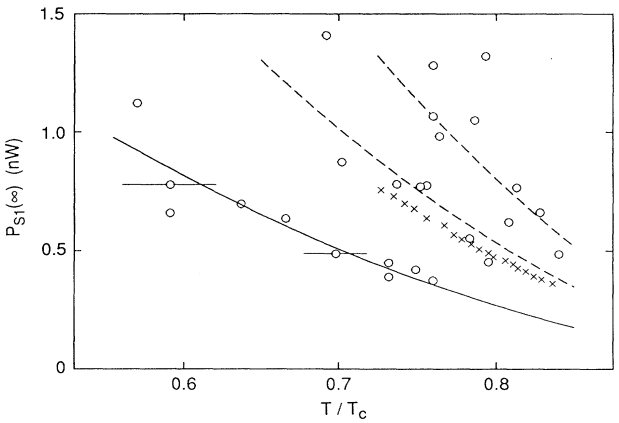


FIG. 12. Saturation value $P_{S1}(\infty)$ of the $\Omega$-dependent component of the additional absorption as a function of temperature. The circles are obtained by fitting Eq. (14) to the measurements of $P_{S1}(\Omega)$ in metastable states with different numbers of solitons in the counterflow zone. Our interpretation is that the lowest set of points, through which the solid line is drawn, corresponds to one soliton. Dashed lines would then show, respectively, $P_{S1}(\infty)$ for two and three solitons in the counterflow region. Crosses depict the additional absorption $P_S(\Omega = 2.0\,\mathrm{rad/s})$ observed in an experiment, during which the sample warmed at constant $\Omega$. During these measurements, $p = 29.3$ bars, $H = 14.2$ mT, $\nabla H = 4 - 6$ mT/m, and $\mathbf{H} \parallel \mathbf{\Omega}$.

duced from the total absorption $P_S(\Omega)$, from which we subtracted the weakly $\Omega$ dependent component $P_{S2}$ that remained after annihilation of solitons in the counterflow region.

The distribution of $P_{S1}(\infty)$ is interpreted as follows: the lowermost branch, which is depicted by the solid line, shows the saturation value of $P_{S1}(\Omega)$ in the case when there is only one $\theta$ soliton in the counterflow region. The dashed lines illustrate the same $P_{S1}(\infty)$ multiplied by 2 and 3, and would thus correspond to two and three solitons. These higher branches do not show up as clearly as the lowest one in the measured data: the relative uncertainty in the determination of $P_{S1}(\infty)$, about $\pm 20\%$, is roughly the same for every point in Fig. 12 and becomes, in the case of three solitons, comparable to the separation between the branches. The scatter is mainly caused by the uncertainties in $\nabla H$ and in the weakly $\Omega$-dependent component $P_{S2}$. The crosses in the figure depict $P_S(T, \Omega = 2.0\,\mathrm{rad/s})$ during an experiment, in which the sample was warming up at constant $\Omega$. The high-$T$ end of the solid line was drawn using the temperature dependence in this set of data.

The temperature for each point in Fig. 12 was measured, after the additional absorption had decayed, by determining the magnetization from the HPD signal. The total voltage induced in the pick-up coil from the HPD is proportional to the magnetization $M(T) = \chi_B(T)H$. The measured voltage was compared with the corresponding value at $T_{AB}$ and, by using the susceptibility data from Ref. 43 and the ratio $T_{AB}/T_c$ from Ref. 38, we obtained the temperature. The uncertainty arising from this procedure increases rapidly toward lower temperatures and is shown by the error bars in Fig. 12.

### C. Annihilation of solitons in the vortex cluster

In a few experiments, $P_S$ was seen to decay with discontinuous downward jumps of equal magnitude, which could be interpreted as annihilation of individual solitons inside the vortex cluster. These processes happened either spontaneously or they could be induced by sudden changes in $\Omega$. Figure 13 shows four spontaneously occurring steps in the HPD absorption, recorded at constant $\Omega$. To prove that they originated from the cluster, and not from the solitons in the counterflow layer, we did the following check: After observing seven steps of magnitude $\Delta P_S = 19.8 \pm 3.0$ pW, the rotation velocity was increased from $\Omega_{AB} = 1.0$ rad/s to $\Omega = 1.6$ rad/s. At this higher $\Omega$, two more jumps of $\Delta P_S = 16.5$ pW were seen. During acceleration, the counterflow layer widens, so that if the steps would have originated from the annihilation of solitons in the counterflow layer, we would have expected to see a 50% increase in the steps. Instead, $\Delta P_S$ decreased.

The size distribution of the absorption steps during one experiment is shown in the insert of Fig. 14. There is a clear preference for $\Delta P_S \approx 30$ pW; the two events of higher $\Delta P_S$ are interpreted as simultaneous annihilations of two and three solitons, respectively. In the main part of Fig. 14 we have collected data from the runs during

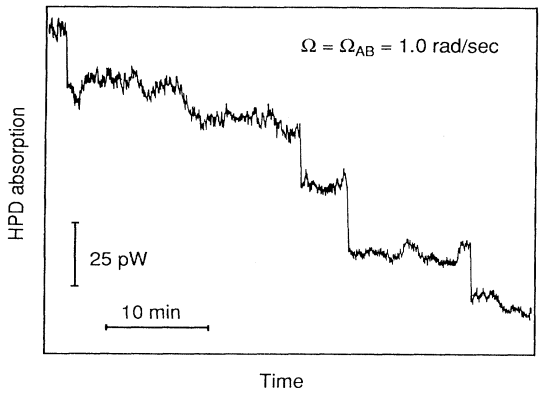


FIG. 13. Stepwise decay of the soliton absorption $P_S$. The HPD absorption signal, measured at constant $T$ and $\Omega$, exhibits four equal downward jumps, which are interpreted to show disappearances of solitons in the vortex cluster. Here the annihilations occur spontaneously, but they can also be induced by a rapid change in $\Omega$. This experiment was done at $p = 29.3$ bars, $T = 0.52T_c$, $H = 14.2$ mT, $\nabla H = 5$ mT/m, and $\mathbf{H} \parallel \mathbf{\Omega}$.

which annihilation of solitons was observed. Each point corresponds to a different cooldown from the $A$ phase and represents the average $\Delta P_S$ from 3 to 13 events, observed at stable temperature. The temperature for every point was again measured by determining the magnetization from the HPD signal. At $0.6T_c$, the absorption from one soliton inside the vortex cluster corresponds to the absorption from $2 \times 10^3$ axisymmetric vortices. In our cell this number of vortices is reached in the equilibrium

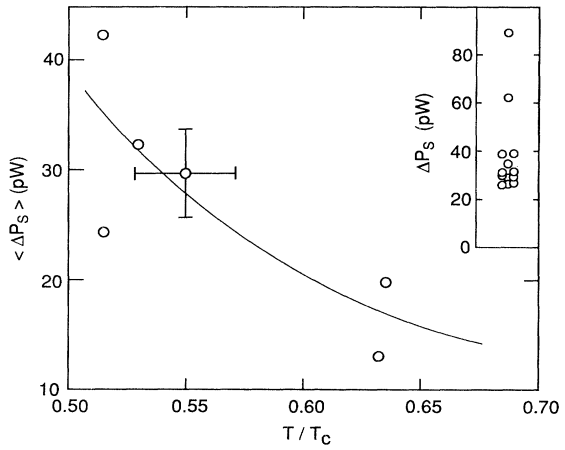


FIG. 14. Magnitude of the absorption steps, caused by solitons annihilated inside the vortex cluster, as a function of temperature. Each data point is an average of 3 to 13 events, measured at stable temperature, which is known with the accuracy indicated by the error bar. The vertical error bar shows the standard deviation within one set of absorption steps. The line is guide for the eyes. The insert shows the distribution of step sizes in the annihilations during an experiment, which was done at $T = 0.55T_c$. In these measurements, $p = 29.3$ bars, $\Omega = 1.0$ rad/s, $H = 14.2$ mT, $\nabla H = 5$ mT/m, and $\mathbf{H} \parallel \mathbf{\Omega}$.

state at $\Omega = 2$ rad/s.

The magnitudes of absorption, $P_{S1}$ from solitons in the counterflow layer and $P_{S2}$ from solitons in the vortex cluster, are in reasonable agreement with each other and with the absorption $P_B$ in the free HPD boundary at $\Omega = 0$. The measured $P_{S1}(\infty)$ corresponding to the maximum width $\ell = R = 3.5$ mm of a soliton, is 0.5 nW in a field of 14.2 mT, with $\nabla H = 5\,\mathrm{mT/m}$ and at $T = 0.7\,T_c$. For the same parameter values, the measured $P_{S2}$, induced by a single soliton in the cluster, is about 0.015 nW and $P_B = 0.05$ nW ($P_B$ is measured in Ref. 42). On the basis of the discussion in Sec. VIII C [see Eq. (15)], we expect to have $P_{S1}(\infty) \propto 2 \times \frac{2}{3} D M^2 R (L/\lambda_0)^{3/2}$, where the factor 2 is because of the two HPD-NPD interfaces of the soliton. This value should be compared with the absorption from the boundary $P_B \propto D M^2 \pi R^2/\lambda_0$, where $\lambda_0$ is the width of the free boundary. In the above mentioned conditions, $\lambda_0$ is about 0.3 mm, which gives $P_{S1}(\infty)/P_B \sim 4$. Estimation of $P_{S2}$ for a soliton in the vortex cluster gives $P_{S2}/P_B \sim L/(\pi R^2/\lambda_0) \sim 0.1$. The measured ratio, $P_B{:}P_{S2}{:}P_{S1}(\infty) = 10{:}3{:}100$, compares well with the ratio expected from the above order of magnitude estimations 10:1:40.

Dependence of $P_S$ on the magnitude of the magnetic field might give important information on soliton absorption. Comparison of the measurements in Fig. 8 ($H = 28.4$ mT, $\nabla H = 1.5$ mT/m) with the results in Fig. 12 ($H = 14.2$ mT, $\nabla H \approx 5$ mT/m) gives the ratio $P_{S1}(\infty, 28.4\ \mathrm{mT})/P_{S1}(\infty, 14.2\ \mathrm{mT}) \approx 3.5$, if it is assumed that $P_{S1}(\infty) \propto \sqrt{\nabla H}$ and that only a single soliton in the counterflow layer is present in the anomalous states in Fig. 8. In Fig. 8, $P_{S2}$ appears to be by a factor 2.5 larger than in Fig. 14. These comparisons do not severely contradict our model of the source for $P_S$ which predicts that $P_{S2}(H) \propto H^2$ and $P_{S1}(H) \propto H^{5/2}$. The number of our measurements in the higher field is quite limited, and we cannot at present make very conclusive statements about $P_S(H)$.

The temperature dependence of $P_S$ remains unexplained. It should be noted that the absorption at the free HPD boundary increases toward higher temperatures,[42] whereas $P_S$ in Figs. 12 and 14 shows an opposite tendency. The apparent contradiction may be explained by different orientations of the HPD boundaries in the two cases.

## X. SUMMARY

We have studied a rotating $B$-phase state which is created during cooldown at constant rotation velocity through reversible $A \rightarrow B$ phase transition. The state has anomalous NMR signatures, which can be explained by introducing a new type of topological object: a spin-mass vortex which is bound to a planar soliton. It is argued theoretically, that SMV's provide a unique explanation of the observations. Thus the number of different line defects which have been observed in superfluid $^3$He-$B$ has increased to three: There are two mass vortices with different structures of the core and the spin-mass vortex.

## ACKNOWLEDGMENTS

We wish to thank V.V. Dmitriev, O.V. Lounasmaa, and Ü. Parts for discussions and/or help with the measurements. This work has been supported by the Körber Stiftung (Hamburg, Germany) and through the ROTA cooperation project between the Academy of Finland and the USSR Academy of Sciences.

## APPENDIX: SYMMETRY APPROACH TO THE HPD

Let us first assume that (i) the frequency of the rf field $\omega$ exactly coincides with the Larmor frequency $\omega_0$ and (ii) the dipole interaction (6) is neglected. Then there is no preferred direction for the magnetization and for the order parameter in a frame precessing at $\omega_0$. This follows from the Larmor theorem, which states that the effect of the magnetic field on the spins completely disappears in a system rotating with the Larmor frequency.

The total symmetry group of the physical laws for the system precessing with the Larmor frequency is

$$\tilde{G} = \mathrm{U}(1) \times \mathrm{SO}_3^{\tilde{S}} \times \mathrm{SO}_3^{L} \ , \tag{A1}$$

where $\mathrm{SO}_3^{\tilde{S}}$ is the group of spin rotations in the precessing frame. The Larmor theorem implies that $\tilde{G}$ is isomorphic with $G$ (1). As in Sec. II A we can introduce the matrices $\underline{R}^{(1)}$ and $\underline{R}^{(2)}$ of spin and orbital rotations, but now we must take into account that $\underline{R}^{(1)}$ is the matrix of spin rotations in the precessing frame. In the laboratory frame, the $\mathrm{SO}_3^{\tilde{S}}$ symmetry operation becomes time dependent, viz.,

$$\underline{O}(\hat{\mathbf{z}}, \omega t)\ \underline{R}^{(1)}\ \underline{O}(\hat{\mathbf{z}}, -\omega t) \ . \tag{A2}$$

Here $\underline{O}(\hat{\mathbf{z}}, \omega t)$ is the transformation from the laboratory frame into the rotating frame; it is a rotation about the axis $\hat{\mathbf{z}} \parallel \mathbf{H}$ by an angle $\omega t$. Equation (A2) means that in order to produce the $\mathrm{SO}_3^{\tilde{S}}$ symmetry transformation, one should first make the transformation from the laboratory frame into the precessing frame, then make the $\underline{R}^{(1)}$ rotation within this frame, and finally return back to the laboratory frame.

We can find all the degenerate coherent states by applying the symmetry group (A1) to some initial state. Since we are interested in states degenerate with the equilibrium state, we choose the simplest equilibrium state

$$A_{\alpha i}^{(0)} = \Delta_B\ \delta_{\alpha i} \ , \quad \mathbf{M}^{(0)} = \chi_B \mathbf{H} \ . \tag{A3}$$

The action of elements of group $\tilde{G}$ on this state, $\underline{A} = \underline{O}\,\underline{R}^{(1)}\underline{O}^{-1}\underline{A}^{(0)}(\underline{R}^{(2)})^{-1}$, leads to the following general time-dependent state:

$$A_{\alpha i}(t) = \Delta_B\ e^{i\Phi}\ R_{\alpha i}(t) \ , \tag{A4}$$

$$R_{\alpha i}(t) = O_{\alpha\beta}(\hat{\mathbf{z}}, \omega t) R^{(1)}_{\beta\gamma} O_{\gamma\mu}(\hat{\mathbf{z}}, -\omega t)(R^{(2)})^{-1}_{\mu i} \ . \tag{A5}$$

The magnetization in this state is obtained by the rotation $\mathrm{SO}_3^{\tilde{S}}$ from the initial $\mathbf{M}$ in Eq. (A3), viz.,

$$M_\alpha(t) = \chi_B O_{\alpha\beta}(\hat{\mathbf{z}}, \omega t) R^{(1)}_{\beta\gamma} H_\gamma \ . \qquad \text{(A6)}$$

This means that the magnetization in the precessing frame is constant in time.

Equations (A5) and (A6) represent the general solution of the Leggett equations [29] for the spin dynamics under the conditions (i) $\omega = \omega_0$ and (ii) the dipole interaction is absent. The large degeneracy of the Larmor precession is reduced if these constraints are lifted. We first include the dipole interaction because it is the dominant one in the present experiments. The dipole energy (6) has its minimum when $\theta = \theta_L$. This is possible for two groups of degenerate states. The first family has $\underline{R}^{(1)} \equiv \underline{1}$. Thus the matrix $R_{\alpha i}(\hat{\mathbf{n}}, \theta_L)$ given by Eq. (A5) is independent of time and $\mathbf{M}^{(0)} = \chi_B \mathbf{H}$. These are the equilibrium states discussed in Sec. II. The other family has $\underline{R}^{(2)} \equiv \underline{1}$. These are the precessing states. The validity of Eq. (11) for the precessing states follows from (A5) and (A6). The generalization to $\omega \neq \omega_0$ is made in Sec. IV A.

* Present address: Physics Department, University of Kyoto, Kyoto, Japan.
† Present address: Physics Department, University of Bayreuth, 8580 Bayreuth, Germany.
‡ Also at Landau Institute for Theoretical Physics, 117334 Moscow, USSR.

[1] P.J. Hakonen, O.V. Lounasmaa, and J.T. Simola, Physica B **160**, 1 (1989).
[2] E.V. Thuneberg, Phys. Rev. B **36**, 3583 (1987); M.M. Salomaa and G.E. Volovik, Rev. Mod. Phys. **59**, 533 (1987); **60**, 573(E) (1988).
[3] P.J. Hakonen and K.K. Nummila, Phys. Rev. Lett. **59**, 1006 (1987); J.S. Korhonen, A.D. Gongadze, Z. Janu, Y. Kondo, M. Krusius, Yu.M. Mukharskiy, and E.V. Thuneberg, *ibid.* **65**, 1211 (1990).
[4] Y. Kondo, J.S. Korhonen, Ü. Parts, M. Krusius, O.V. Lounasmaa, and A.D. Gongadze, Physica B **178**, 90 (1992).
[5] A.S. Borovik-Romanov, Yu.M. Bunkov, V.V. Dmitriev, Yu.M. Mukharsky, and K. Flachbart, Zh. Eksp. Teor. Fiz. **88**, 2025 (1985) [Sov. Phys. JETP **61**, 1199 (1985)].
[6] I.A. Fomin, Zh. Eksp. Teor. Fiz. **88**, 2039 (1985) [Sov. Phys. JETP **61**, 1207 (1985)].
[7] A.S. Borovik-Romanov, Yu.M. Bunkov, V.V. Dmitriev, Yu.M. Mukharsky, E.V. Poddyakova, and O.D. Timofeevskaya, Zh. Eksp. Teor. Fiz. **96**, 956 (1989) [Sov. Phys. JETP **69**, 542 (1989)].
[8] Yu.M. Bunkov and P.J. Hakonen, J. Low Temp. Phys. **83**, 323 (1991).
[9] J.S. Korhonen, V.V. Dmitriev, Z. Janu, Y. Kondo, M. Krusius, and Yu.M. Mukharsky, Physica B **165&166**, 671 (1990).
[10] V.V. Dmitriev, Y. Kondo, J.S. Korhonen, M. Krusius, Yu.M. Mukharsky, E.B. Sonin, and G.E. Volovik, Physica B **165**, 655 (1990); Y. Kondo, J.S. Korhonen, M. Krusius, V.V. Dmitriev, Yu.M. Mukharsky, E.B. Sonin, and G.E. Volovik, Phys. Rev. Lett. **67**, 81 (1991).
[11] V.P. Mineev and G.E. Volovik, Phys. Rev. B **18**, 3197 (1978).
[12] K. Maki and P. Kumar, Phys. Rev. B **14**, 118 (1976).
[13] Y. Kondo, J.S. Korhonen, M. Krusius, V.V. Dmitriev, E.V. Thuneberg, and G.E. Volovik, Phys. Rev. Lett. **68**, 3331 (1992).
[14] L.D. Landau and E.M. Lifshitz, *Statistical Physics, Part 1* (Pergamon, Oxford, 1980).
[15] D. Vollhardt and P. Wolfle, *The Superfluid Phases of Helium 3* (Taylor and Francis, London, 1990).
[16] K. Maki and P. Kumar, Phys. Rev. B **16**, 4805 (1977).
[17] O. Ishikawa, Y. Sasaki, T. Mizusaki, A. Hirai, and M. Tsubota, J. Low Temp. Phys. **75**, 35 (1989).
[18] D.D. Osheroff, in *Quantum Fluids and Solids*, edited by S.B. Trickey, E.D. Adams, and J.W. Dufty (Plenum, New York, 1977), p. 161.
[19] P.J. Hakonen, M. Krusius, M.M. Salomaa, R.H. Salmelin, J.T. Simola, A.D. Gongadze, G.E. Vachnadze, and G.A. Kharadze, J. Low Temp. Phys. **76**, 225 (1989).
[20] G.E. Volovik and V.P. Mineev, Zh. Eksp. Teor. Fiz. **72**, 2256 (1977) [Sov. Phys. JETP **45**, 1186 (1977)].
[21] N.D. Mermin, Rev. Mod. Phys. **51**, 591 (1979).
[22] See, for example, M. Vuorio, J. Phys. C **7**, L5 (1974).
[23] E.V. Thuneberg, Europhys. Lett. **3**, 711 (1987).
[24] The simplest way of joining of the structures at $r \ll \xi_D$ and $r \gg \xi_D$ is obtained if $\hat{\mathbf{n}}$ at $r \ll \xi_D$ is the same as in the soliton wall.
[25] O.D. Lavrentovich and S.S. Rozhkov, Pis'ma Zh. Eksp. Teor. Fiz. **47**, 210 (1988) [JETP Lett. **47**, 254 (1988).
[26] A. Vilenkin, Phys. Rep. **2**, 263 (1985).
[27] G.E. Volovik, Pis'ma Zh. Eksp. Teor. Fiz. **52**, 972 (1990) [Sov. Phys. JETP Lett. **52**, 358 (1990)].
[28] W.F. Brinkman, H. Smith, D.D. Osheroff, E.I. Blount, Phys. Rev. Lett. **33**, 624 (1974).
[29] A. J. Leggett, Ann. Phys. (N.Y.) **85**, 11 (1974).
[30] T. Sh. Misirpashaev and G.E. Volovik, Zh. Eksp. Teor. Fiz. **102**, 1197 (1992) [Sov. Phys. JETP **75**, 650 (1992)].
[31] I. Fomin, Zh. Eksp. Teor. Fiz. **94**, 112 (1988) [Sov. Phys. JETP **67**, 1148 (1988)]; A.S. Borovik-Romanov, Yu.M. Bunkov, V.V. Dmitriev, Yu.M. Mukharsky, and D.A. Sergatskov, in *Quantum Fluids and Solids-1989*, edited by G. Ihas and Y. Takano, AIP Conf. Proc. No. 194 (AIP, New York, 1989), p. 27; Physica B **165&166**, 649 (1990).
[32] Yu.M. Bunkov and O.D. Timofeevskaya, Pisma Zh. Eksp. Teor. Fiz. **54**, 232 (1991) [JETP Lett. **54**, 228 (1991)].
[33] A.J. Leggett and S. Takagi, Phys. Rev. Lett. **34**, 1424 (1975).
[34] P.J. Hakonen, O.T. Ikkala, S.T. Islander, O.V. Lounasmaa, T.K. Markkula, P. Roubeau, K.M. Salomaa, D.I. Garibashvili, and J.S. Tsagadze, Cryogenics **23**, 243 (1983).
[35] Ü. Parts, Y. Kondo, J.S. Korhonen, M. Krusius, E.V. Thuneberg, and G.E. Volovik (unpublished).
[36] G.E. Volovik, Physica B **178**, 160 (1992).
[37] E.V. Thuneberg, Physica B **178**, 168 (1992).
[38] D.S. Greywall, Phys. Rev. B **33**, 7520 (1986).
[39] D.S. Buchanan, G.W. Swift, and J.C. Wheatley, Phys. Rev. Lett. **57**, 341 (1986).
[40] P.J. Hakonen and V.P. Mineev, J. Low Temp. Phys. **67**, 313 (1987).
[41] G. Volovik, Pis'ma Zh. Eksp. Teor. Fiz. **51**, 396 (1990) [JETP Lett. **51**, 449 (1990)]; T. Misirpashaev, Zh. Eksp. Teor. Fiz. **99**, 1741 (1991) [Sov. Phys. JETP **72**, 973 (1991)].
[42] Y. Kondo, J.S. Korhonen, and M. Krusius, Physica B **165**, 673 (1990).
[43] H.N. Scholz, Ph.D. thesis, Ohio State University (1981).